A reinterpretation of the relationship between persistent and resurgent sodium currents

Condensed Title: Na^+ currents role in repetitive neuronal firing

Samuel P. Brown[1], B.S.; Ryan J. Lawson[1], B.S.; Jonathan D. Moreno, M.D., Ph.D.[2]; Joseph L. Ransdell[1,4], Ph.D.

[1]Department of Biology
Miami University, Oxford, OH 45056

[2]Division of Cardiology, Department of Medicine
Washington University in St. Louis, St. Louis, MO 63130

[4]Correspondence: ransdejl@miamioh.edu

SUMMARY

Across neuronal cell types, the resurgent sodium current (I_{NaR}) is often implicated in driving high rates of repetitive firing. Using dynamic clamp, we determined I_{NaR} is ineffective at driving subsequent action potentials, and that the subthreshold persistent sodium current is the critical parameter for scaling repetitive firing rates.

Abstract

The resurgent sodium current (I_{NaR}) activates on membrane repolarization, such as during the downstroke of neuronal action potentials. Due to its unique activation properties, I_{NaR} is often thought to support high rates of repetitive neuronal firing. However, I_{NaR} is typically studied in combination with the persistent or non-inactivating portion of sodium currents (I_{NaP}). We used dynamic clamp to test how I_{NaR} and I_{NaP} individually affect repetitive firing in adult cerebellar Purkinje neurons. We learned I_{NaR} has no effect on repetitive firing rates due to its rapid decay at subthreshold voltages, and that subthreshold I_{NaP} is critical in regulating neuronal firing rate. Using computational modeling and dynamic clamp experiments, we found I_{NaP} and I_{NaR} can be inversely scaled by adjusting occupancy in a slow inactivated kinetic state. Thus, by reducing Nav channel slow inactivation, I_{NaR} is reduced and I_{NaP} is increased, which drives higher rates of Purkinje neuron firing.

Introduction

Purkinje neurons are the exclusive output cells of the cerebellar cortex, delivering GABA-mediated inhibitory signals to neurons in the deep cerebellar nuclei (Ito, 1984; Ito et al., 1964; Obata et al., 1967, 1970). In the absence of synaptic drive, Purkinje neurons have a unique capacity to fire action potentials repetitively at high frequencies (Häusser & Clark, 1997; Raman & Bean, 1997; Thach, 1968), properties which rely on voltage-gated sodium (Nav) channels and the depolarizing currents these channels mediate (Llinás & Sugimori, 1980; Raman & Bean, 1999; Ransdell & Nerbonne, 2018). Beyond the fast-inactivating transient sodium current (I_{NaT}), Nav channels can generate a persistent or non-inactivating sodium current (I_{NaP}) component, which was first measured and described in cerebellar Purkinje neurons (Llinás & Sugimori, 1980). Nav channels may also generate a resurgent Nav current (I_{NaR}) component, also first characterized in cerebellar Purkinje neurons, which has now been measured in over twenty neuronal cell types throughout the central and peripheral nervous systems (Lewis & Raman, 2014; Raman & Bean, 1997). I_{NaR} is distinct from the transient and persistent Nav currents in that it activates on membrane repolarization. After membrane depolarization, which drives Nav channels to activate/open and undergo fast-inactivation, as the membrane voltage repolarizes, a portion of Nav channels may recover into an open/conducting state (see Figure 1A). This re-opening of fast-inactivated Nav channels enables a 'resurgent' depolarizing influx of sodium ions. In the context of neuronal firing, this repolarization would occur during the downstroke of the action potential.

On its discovery, I_{NaR} was proposed to support high rates of neuronal firing by reducing the Nav channel refractory period (Khaliq et al., 2003; Raman & Bean, 1997, 1999), and this assumption continues to be widely accepted (Quattrocolo et al., 2021; Raman, 2023). During an action potential repolarization, if a subset of Nav channels recover into the open state allowing resurgent Na^+ influx, the depolarizing current should drive subsequent action potentials. After its discovery, perturbations to I_{NaR} were also associated with changes in repetitive firing (Khaliq et al., 2003; Lewis & Raman, 2014; Raman et al., 1997; Ransdell et al., 2017). For instance, targeted knockout of Navβ4, a sodium channel accessory subunit, was found to result in significantly reduced I_{NaR} in mouse cerebellar Purkinje neurons (Ransdell et al., 2017) as well as striatal medium spiny neurons (Miyazaki et al., 2014). In both cell types, Navβ4 deletion was also found to result in reduced repetitive firing rates compared to wild type controls (Miyazaki et al., 2014; Ransdell et al., 2022). In dynamic clamp studies, the addition of a modeled I_{NaR} conductance was shown to scale repetitive firing rates both in cerebellar Purkinje neurons (Ransdell et al., 2017) as well as in zebra finch motor neurons (Zemel et al., 2021), although the Nav conductances used in these studies included a persistent Nav current component (I_{NaP}). The isolated contribution of I_{NaR} to neuronal excitability has not been directly tested in native neurons. Here, we use dynamic clamp and multiple Nav conductance models to systematically assess how adjusting properties of I_{NaR} and I_{NaP} affect the firing properties of mouse cerebellar Purkinje neurons.

We learned that scaling the proportion and/or kinetic properties of I_{NaR} does not significantly affect Purkinje neuron firing frequency, nor does the addition of I_{NaR} meaningfully impact the action potential waveform in Purkinje neurons. Instead, subthreshold I_{NaP} was determined to be the critical parameter in tuning Purkinje neuron repetitive firing rates. Using voltage-clamp simulation studies, we determined I_{NaR} does not influence repetitive firing rates due to its rapid decay at subthreshold voltages. In examining the Nav Markov models, we determined that peak I_{NaR} and I_{NaP} can be inversely scaled by adjusting occupancy in the slow-inactivated kinetic state, an inactivation pathway which is distinct from the conventional fast-inactivation pathway. Combined,

these data suggest I_{NaR} may reflect a population of Nav channels which would, in the absence of slow inactivation, contribute to I_{NaP}; suggesting Nav channel slow-inactivation may function to fine tune the amount of Nav channels that contribute to I_{NaP} in order to regulate repetitive firing rates.

Methods

Animals

All animal experiments were performed in accordance with protocols approved by Miami University Institutional Animal Care and Use Committee (IACUC) guidelines. All experiments utilized C57BL/6J wild type mice 4-8 weeks old.

Preparation of acute cerebellar slices

Mice were anaesthetized using an intraperitoneal injection of 1mL/kg ketamine (10 mg/ml)/xylazine (0.25 mg/ml) cocktail and perfused transcardially with 25 ml cutting solution containing (in mM) 240 sucrose, 2.5 KCl, 1.25 NaH_2PO_4, 25 $NaHCO_3$, 0.5 $CaCl_2$, and 7 $MgCl_2$. The brain was rapidly dissected, superglued to a specimen tube, and submerged in warmed agarose dissolved in cutting solution. The cerebellum was sliced sagittally in ice-cold cutting solution saturated with 95% O_2/5% CO_2 using a Compresstome VF-300 (Precisionary Instruments) at 350 µM thickness. Slices were placed in artificial cerebrospinal fluid (ACSF) containing (in mM) 125 NaCl, 2.5 KCl, 1.25 NaH_2PO_4, 25 $NaHCO_3$, 2 $CaCl_2$, 1 $MgCl_2$, and 25 dextrose (pH 7.4, ~300 mOsm) on stretched nylon for 25 minutes at 33°C and then at room temperature for at least 35 minutes before electrophysiological recordings. Purkinje neurons were identified in the Purkinje neuron layer of sagittal cerebellar sections using a SliceScope Pro 3000 (Scientifica).

Electrophysiological recordings

Whole-cell current-clamp and dynamic clamp recordings were obtained from adult mouse Purkinje neurons (4-8 weeks old) in acutely isolated sagittal cerebellar slices that were constantly perfused with ACSF warmed to ~36°C and continuously bubbled with 95% O_2/5% CO_2. Recording pipettes (boroscilicate standard wall, 1.5 mm outer diameter, 0.86 mm inner diameter) were made using a P-1000 Flaming/Brown Micropipette Puller (Sutter Instruments) and filled with internal solution containing (in mM) 0.2 EGTA, 3 $MgCl_2$, 10 HEPES, 8 NaCl, 4 Mg-ATP, and 0.5 Na-GTP. Patch pipette resistances were 2-4 MΩ. Prior to patching, a junction potential correction of 17.5 mV was applied and pipette tip potentials were zeroed. After a gigaseal was obtained, spontaneous action potentials were recorded using a dPatch Amplifier and SutterPatch software (Sutter Instruments). Input resistance and capacitance calculations were obtained through a whole-cell voltage clamp protocol in which the membrane voltage was stepped from a -80 mV holding potential to -90 mV (for 100 ms) and to -70 mV (for 100 ms) in a second sweep. This voltage-clamp protocol was applied in each cell prior to current-clamp or dynamic clamp measurements. For membrane capacitance, the integrated area of the capacitive transient current was divided by the change in membrane voltage (10 mV) during each sweep. Action potential properties were analyzed using SutterPatch software (Sutter Instruments). Action potential events were detected if a transient change in membrane potential exceeded 20 mV. Threshold potential was calculated in SutterPatch as the membrane potential prior to an action potential event when the dV/dt is >1 mV/100 µs, or when 25% of the maximum action potential dV/dt is reached, whichever is smaller. Action potential duration was calculated as the time interval from the pass of threshold voltage during action potential upstroke until the pass of threshold voltage during

action potential downstroke. Each action potential measurement from a given cell was recorded as the average of the measurement across 20 spontaneous action potentials. Dynamic clamp current injection values, measured during the interspike interval (presented in Figures 5D, 6B), were obtained by measuring the dynamic clamp current injection value 3 ms before the action potential threshold was reached for the subsequent action potential. These measurements were made 1 second into each dynamic clamp recording. Recordings were acquired and analyzed using SutterPatch (Sutter Instruments), Microsoft Excel (Microsoft), and Prism (GraphPad) software.

Markov modeling

A previously developed Markov kinetic state model of Nav channel gating (Ransdell et al., 2022) was used as the base/control model, referred to as the nominal model. To develop the 'I_{NaR} increased', 'I_{NaR} decreased', 'τdecay increased', 'τdecay decreased', 'I_{NaR} reduced', and 'I_{NaP} reduced' models (Figures 2-4), rate constants in the nominal model were altered to cause selective changes in Nav current properties. Each of these models consist of a nine state Markov matrix that includes three closed states (C1, C2, C3), two inactivated-closed states (IC1, IC2), two fast inactivated states (IF1, IF2), a slow inactivated state (IS), and an open state (O). The initial I_{NaR} increased/decreased models (hand-tuned models) presented in Figure 2 were developed by manipulating transition rate constant values. Specifically, the hand-tuned I_{NaR} increased and decreased models were generated by altering rate constant equations (see Table 1) which resulted in voltage dependent rate constant alterations. For instance, the b3s rate constant changed from 0.94767 to 3.76696 at -45 mV in the 'I_{NaR} increased' model and in the 'I_{NaR} decreased' model, the b2 rate constant changed from 0.1081 to 3.884 at -45 mV**.** In order to generate additional models, properties of the originally developed (nominal) model were modified by adjusting values in a parameter optimization algorithm scripted in MATLAB (MathWorks) and previously described in (Moreno et al., 2016; Ransdell et al., 2022). The rate constant values for the nominal and each manipulated model are described in Table 1. To generate the 'I_{NaR} reduced' model (Figure 4), state transition rate calculations a3s, b3s, a2s, and b2s were removed from the Q_Matrix.m script prior to parameter optimization. To generate the 'I_{NaP} reduced' model (Figure 4), the variable (ResT_line) within the Na_Matrix_DrugFree.m script was changed from 0.18678*V + 22.92 to 0.18678*V + 38.00. Additionally, in line 113 the Err_Late minimization variable was multiplied by 200. To generate the 'τ_{decay} decreased' model, the ResT_line variable was changed to 0.18678*V + 38.00. Both Err_ACT and Err_SSA variables in line 113 of the error minimization equation (part of the parameter optimization script) were also multiplied by a value of 10. To generate the 'τ_{decay} increased' model, the ResT_line variable was changed to 0.18678*V + 15.00 and the error minimization variables Err_ACT and Err_SSA were multiplied by 90.

With the above alterations, each model was generated by running a minimization routine using a Nelder-Mead "amoeba" algorithm-based optimization procedure (Lagarias et al., 1998; Moreno et al., 2016; Nelder & Mead, 1965) to determine the final transition rate constants associated with each manipulated model (presented in Table 1). All models were simulated using a sodium reversal potential of 71.5 mV. All kinetic state occupancy simulations and optimizations were completed in MATLAB 2022a. Simulations and current measurements from each model were performed in SutterPatch using a model cell (Sutter Instruments) to verify the Nav currents generated by each model (I_{NaT}, I_{NaR}, and I_{NaP}) had appropriate voltage-dependent and kinetic properties. Currents were evoked in each model using simulated voltage clamp protocols applied to the model cell while the simulated conductance was applied via dynamic clamp through a Sutter

Instruments dPatch amplifier. The voltage dependance of activation of I_{NaT} and I_{NaP} were obtained by stepping the model cell (from a -90 mV holding potential) to -70 mV – 0 mV in 5 mV increments for 80 ms. I_{NaR} voltage-dependence of activation was obtained by stepping the model cell from a holding potential of -90 mV to 0 mV for 5 ms, and then applying a repolarizing step to -70 mV - 0mV (in 5 mV increments) for 80 ms. Prior to analysis of I_{NaT} or I_{NaR}, I_{NaP} was digitally subtracted. MATLAB scripts used for the optimization procedure and the nominal Markov state matrix are available on GitHub: https://github.com/morenomdphd/Resurgent_INa.

Action potential clamp gating simulations

To visualize gating state probability over time with an action potential as the voltage command, the MATLAB script Fig_4H_4I.m was adjusted (Ransdell et al., 2022). Prior to plotting, the parameter optimization procedure (see previous section) was run to populate the MATLAB workspace with the required variables. An action potential recording, captured from an adult mouse Purkinje neuron firing spontaneous action potentials (at 60.8 Hz) was exported to a Microsoft Excel spreadsheet that contained the time and voltage values of the action potential record. The AP-clamp script was utilized as follows: The script loaded the excel file, which was iterated through the Q_Matrix.m script using the voltage values as the voltage command and the time values as the length of the protocol. Through this script, the values for each gating state as well as I_{Na} and the voltage command were written to the NASIM matrix and then were plotted over time.

Hodgkin-Huxley modeling

A previously developed Hodgkin-Huxley (HH) model of I_{NaP} in Golgi cells was adopted for dynamic clamp experiments (Solinas et al., 2007) and is available on SenseLab ModelDB (ID: 112685). The conductance value of 3.4 nS was selected because peak HH-generated I_{NaP} values were similar to the peak I_{NaP} from nominal model-generated values at 400 nS conductance. The alpha and beta values for the HH I_{NaP} model can be found in the table below.

α	**β**
5/((0.0421*(V+50)/(1-exp(-1*(V+50)/5)))+(-0.287*(V+50)/(1-exp((V+50)/5))))	1/(1+exp(-1*(V+53)/5))

Dynamic clamp

Modeled conductances were applied to whole-cell-patched adult mouse Purkinje neurons through SutterPatch software and a dPatch amplifier. Markov model conductances were applied in dynamic clamp experiments using a sodium reversal potential of 71.5 mV and a conductance value of 400 nS. The Hodgkin Huxley model, described above, was applied using the same reversal potential and 3.4 nS conductance. In all dynamic clamp experiments, a model conductance was only applied after a gap-free current clamp recording (10 second duration) of action potential firing (with dynamic clamp turned off). These intermittent recordings (between applications of model Nav conductances) served as control measurements of Purkinje neuron firing rate without the addition of a model Nav conductance. In all cells included in the analysis, baseline repetitive firing frequencies, with no dynamic clamp current injection, did not vary by more than 10% throughout the duration of the experiment.

Results

Dynamic clamp addition of a modeled Nav conductance increases the spontaneous firing frequency of adult cerebellar Purkinje neurons

Purkinje neuron voltage-gated sodium (Nav) currents include fast-transient (I_{NaT}), persistent (I_{NaP}), and resurgent (I_{NaR}) components, which can be isolated and measured using steady state voltage-clamp steps. Voltage-clamp records presented in Figure 1A (*middle traces*) were acquired from an acutely isolated Purkinje neuron (P16) and reflect the I_{NaT} and I_{NaR} components. A brief depolarizing voltage step to 0 mV (from a -90 mV holding potential) activate Nav channels, the majority of which quickly inactivate resulting in the transient Nav current (I_{NaT}), and a repolarization voltage step to more negative potentials enable a portion of the fast-inactivated Nav channels to recovery into an open/conducting state, which results in 'resurgent' sodium influx (I_{NaR}). I_{NaR} (at fixed voltages) decays much slower than I_{NaT}. At voltages that enable peak I_{NaR} activation (typically around -45 mV), the time constant of I_{NaR} decay is ~12 ms, and at more hyperpolarized voltages, the time constant of I_{NaR} decay falls to 2-3 ms (Raman & Bean, 1997; Zemel et al., 2021). I_{NaR} decay eventually results in a steady-state depolarizing Nav current in which a population of Nav channels remain in the open/conducting state. This remaining persistent current component reflects I_{NaP}. I_{NaR} was first measured in cerebellar Purkinje neurons (Raman & Bean, 1997) and because I_{NaR} is a depolarizing current activated by membrane repolarization, such as the downstroke of an action potential, this depolarizing Nav current is hypothesized to be associated with supporting high rates of repetitive firing. To test this role directly, we used a Markov kinetic state model (depicted in Figure 1B), which accurately reproduces the voltage and time dependent properties of Purkinje neuron Nav currents (Ransdell et al., 2022), to test directly how I_{NaR} properties affect Purkinje neuron repetitive firing. Development of the Nav conductance model is published in Ransdell et al. (2022) and is based on Nav current properties recorded from C57bl/6 mouse Purkinje neurons. The kinetic state Markov model has a single open/conducting state along with two parallel inactivation pathways which are separated as fast (IF1+IF2) and slow (IS) inactivation kinetic states.

To test and verify the dynamic clamp configuration (depicted in Figure 1C), we used SutterPatch dynamic clamp software to apply the model Nav conductance to a passive model cell (Sutter Instruments). Voltage-clamp commands were applied to the model cell with the Markov model conductance added using dynamic clamp software, and the model-generated currents were recorded. Nav currents generated by this conductance model had similar voltage-dependent and kinetic properties as those measured in mouse Purkinje neurons (Ransdell et al., 2022). Figure 1A bottom current traces show the performance of the Nav conductance model under an identical voltage command. The nominal conductance model produces $I_{NaT,}$ I_{NaR}, and I_{NaP} current components. We utilized this model throughout our dynamic clamp experiments as a baseline addition of Nav conductance and refer to it as the 'nominal' model throughout the rest of this manuscript. We applied the nominal model conductance to adult (4-7-week-old) Purkinje neurons in acute sagittal brain slices at physiological temperatures. The nominal model applied at 400 nS (see Methods) significantly ($P < 0.0001$, paired Student's t-test, $n = 30$) increased the spontaneous firing frequency of Purkinje neurons, compared to spontaneous firing without dynamic clamp (Figure 1E). Addition of the nominal model conductance also resulted in significant ($P < 0.001$, RM one-way ANOVA, $n = 24$) increases in evoked firing frequency during depolarizing current injections (see Supplementary Figure 1).

Adjusting peak I_{NaR} does not scale the repetitive firing frequency of Purkinje neurons

We developed and tested Nav conductance models that have varying levels of peak I_{NaR}. To alter peak I_{NaR}, individual rate constants in the nominal Markov model (presented in Figure 1) were adjusted. By increasing the rate constant b2, which is responsible for transiting channel occupancy from the fast-inactivated state into the open state, peak I_{NaR} was increased to a peak value of 1.38 nA (measured at -45 mV), compared to 680 pA in the nominal model (see Figure 2A, B, *green*). Alternatively, by increasing the b3s rate constant, which is responsible for transiting channel occupancy from the closed state into the slow inactivated state, peak I_{NaR} was reduced to 350 pA (measured at -45 mV) (Figure 2A, B, *red*). Voltage-clamp records of Nav currents produced by these models, along with peak I_{NaR} I-V plots for these models are shown in Figures 2B, and C. Model-generated Nav currents were produced using a 400 nS conductance value. To test how scaling I_{NaR}, using these new models, affects the repetitive firing properties of Purkinje neurons, we added the model variants to Purkinje neurons using dynamic clamp. The nominal model, along with the 'I_{NaR} decreased' (*red*) and 'I_{NaR} increased' (*green*) models were applied to the same Purkinje neurons also using 400 nS conductance for each model. Consistent with the hypothesis that I_{NaR} supports high rates of repetitive firing, we found adding the 'I_{NaR} reduced' model conductance resulted in significantly reduced repetitive firing frequencies compared to addition of the nominal model conductance (Figure 2D, *left*). However, when the 'I_{NaR} increased' conductance model was added, there was no significant change in the repetitive firing rates compared to addition of the nominal model conductance (Figure 2D, *right*). The 'I_{NaR} increased' conductance model has a peak I_{NaR} value that is 2.3 times larger than the nominal model (see Figure 2C). We reasoned that additional Nav current properties, other than peak I_{NaR}, were likely altered in creating the 'I_{NaR} increased' and 'I_{NaR} decreased' models, which may have influenced the effects of each model conductance on repetitive firing frequencies. Analysis of the voltage-clamp simulation traces revealed the time constant of I_{NaR} decay was reduced in both the 'I_{NaR} decreased' and 'I_{NaR} increased' models, compared to the nominal model. Additionally, we noted I_{NaP} was much smaller in the 'I_{NaR} reduced' model compared to the nominal model. Measures of these Nav current components are presented under the I-V plot in Figure 2C.

Purkinje neuron repetitive firing rates are not affected by adjusting the time constant of I_{NaR} decay

Because altering a single rate constant was found to alter multiple Nav conductance parameters, notably the tau of I_{NaR} decay and the proportion of I_{NaP}, we utilized a numerical optimization procedure (see schematic in Fig. 3A and description in Methods) to develop additional Nav conductance Markov models that exhibit targeted changes to the nominal model, while working to conserve other Nav conductance parameters in the nominal model. Our first goal was to selectively alter the tau of I_{NaR} decay. To develop models with either a longer or shorter I_{NaR} decay, compared to the nominal model, we adjusted the constraint for the decay of I_{NaR} before applying the rate constant optimization (amoeba method) procedure. This strategy allowed us to develop two new conductance models that compared to the nominal model in Figure 3B-C, have a tau of I_{NaR} decay that is either longer ('τdecay increased', *blue*) or shorter ('τdecay decreased', *green*). The time constant of I_{NaR} decay is plotted against voltage for each model in Figure 3B. While these models have different peak I_{NaT}, I_{NaP}, and I_{NaR} values (using a 400 nS conductance) than the nominal model (see Figures 3C1-C3), the values of these current components were similar to one another. This enabled us to test the effect of altered I_{NaR} decay rates directly using dynamic clamp experiments.

When the two newly developed models, 'τdecay increased' and 'τdecay decreased' were added at 400 nS to adult Purkinje neurons, both models were found to cause significant increases in repetitive firing, compared to no model (see Supplemental Figure 2C, D). However, the increased repetitive firing rates (under both models) were not significantly different from one another (Figure 3D, E), indicating that while adding the modeled Nav conductance increases repetitive firing rates, applying substantial changes to the tau of I_{NaR} decay does not affect these firing rates (see Figure 3D). We noted that both of the new models resulted in significantly lower firing rates than the nominal model (Figure 3E). We also noted the 'τdecay increased' and 'τdecay decreased' models generate lower peak I_{NaP} values than the nominal model (Figure 3C2).

Peak I_{NaP}, not peak I_{NaR}, is critical in scaling Purkinje neuron repetitive firing rates.

We hypothesized that I_{NaP} may be a critical determinant in scaling repetitive firing rates in Purkinje neurons. To test this hypothesis, we employed a constrained numerical optimization method, (presented in Figure 4) to constrain the proportion of I_{NaP} in order to significantly reduce peak I_{NaP} while leaving other Nav current components intact. This model is referred to as the 'I_{NaP} reduced' model. Even utilizing numerical optimization methods, it was difficult to develop the 'I_{NaP} reduced' model without significantly reducing peak I_{NaR} values (Figure 4A1). For this reason, we developed an additional model which has similar levels of I_{NaP} and I_{NaT} as the nominal model (Figure 4A2, 4A3), but that also has a reduced peak I_{NaR} compared to the nominal model (Figure 4A1). Dynamic clamp-mediated addition of these models could then be used to isolate the effects of reduced I_{NaP} on Purkinje neuron firing by comparing the effects of both models, 'I_{NaR} reduced' and 'I_{NaP} reduced', to the effects of the nominal model. Results from these dynamic clamp studies, presented in Figure 4B, C, reveal addition of the 'I_{NaP} reduced' model results in significantly lower repetitive firing rates than the addition of the nominal model (Figure 4C, *right*), while adding the 'I_{NaR} reduced' model conductance has no significant effect on firing rates compared to addition of the nominal model conductance (Figure 4C, *left*). Similar to previous experiments, all three models caused a significant increase in repetitive firing frequency when compared to no model/zero pS conductance (see Supplementary Figure 2).

Applying or subtracting I_{NaP} conductance alone scales repetitive firing

The nominal model, and subsequent iterations of the Nav conductance models developed in Figures 3 and 4, have a persistent component that activates maximally at around -60 mV (see Figures 3C2, 4A2). However, I_{NaP} measured in Purkinje neurons typically activates at more depolarized voltages, with peak persistent currents evoked at around -40 mV (Ransdell et al., 2017). To test how this shift in the voltage-dependence of I_{NaP} activation affects the contribution of I_{NaP} to repetitive firing in Purkinje neurons, and to also examine how sole application of I_{NaP} affects repetitive firing in Purkinje neurons, we utilized an I_{NaP} Hodgkin-Huxley (HH) model (previously published in Solinas et al., 2007) for dynamic clamp experiments. We tested the I_{NaP} HH model using voltage-clamp simulations and adjusted the conductance of the model to identify the conductance (3.4 nS) at which the peak I_{NaP} values of the HH model match the peak I_{NaP} values originally measured from the nominal model (see Figure 5A, B). The HH I_{NaP} conductance model applied in dynamic clamp using 3.4 nS conductance was found to be sufficient to increase Purkinje neuron repetitive firing frequency (Figure 5C, *left*). Additionally, we tested if subtracting this conductance via dynamic clamp reduces repetitive firing. We found that dynamic clamp-mediated subtraction of I_{NaP} results in a significant reduction in repetitive firing frequency (Figure 5C, *right*). As is evident in Figure 5C, the HH I_{NaP} conductance, applied across cells at either 3.4 nS or -3.4 nS, has variable effects on firing frequency. In some cells, adding 3.4 nS I_{NaP} caused

only slight increases in firing frequency, while in other cells, adding this conductance drove a nearly 3-fold increase in firing frequency.

We investigated if passive membrane properties might influence the contribution of I_{NaP} to firing frequency. No correlation was found between the input resistance of the cell or its capacitance with the increase or decrease in firing frequency after applying 3.4 nS or -3.4 nS, respectively, of the I_{NaP} conductance model (data not shown). However, dynamic clamp current injection values during the interspike interval, measured 3 ms prior to action potential threshold (see Methods), were found to correlate with the percent increase or decrease in firing frequency after applying the 3.4 nS I_{NaP} model ($r^2 = 0.68$) or -3.4 nS I_{NaP} model ($r^2 = 0.36$), respectively. These data suggest the steady-state depolarizing current provided by I_{NaP} during interspike intervals is a critical determinant in scaling the repetitive firing rates of Purkinje neurons. Because the same conductance values were used across cells, these data also indicate the membrane potential during the interspike interval impacts how the persistent sodium conductance will affect repetitive firing rate.

When applied using dynamic clamp, peak Nav current components (I_{NaT}, I_{NaR}, and I_{NaP}) do not correlate with changes in the action potential waveform.

Application of the nominal model to spontaneously firing Purkinje neurons resulted in significant alterations to the action potential duration (increased), peak (increased), amplitude (increased), and threshold voltage (decreased) (see Table 2). The amplitude of the action potential after-hyperpolarization and the maximum dV/dt, taken from a first derivative phase plot of the action potential waveform, were not significantly affected by applying the nominal model conductance (Table 2). Other Markov conductance models had varying effects on these action potential properties. To test if the magnitude of the Nav current components (I_{NaT}, I_{NaR}, and I_{NaP}), measured across models, scales or consistently alters a given action potential property, we plotted the current value of I_{NaT}, I_{NaR}, and I_{NaP} from each Markov model against the mean change in the action potential parameter after addition of the respective model. These plots (shown in Supplementary Figure 3) indicate the size of these Nav current components across models do not consistently affect or scale any of the measured parameters of the action potential waveform.

Across dynamic clamp Nav conductance models, I_{NaP} is positively correlated with changes in repetitive firing frequency.

Using a similar approach as Figure 5D, we examined how dynamic clamp current injection values relate to changes in repetitive firing frequency across Markov Nav conductance models. We reasoned that during application of a model conductance, the contribution of I_{NaP} is most apparent during the interspike interval immediately preceding the subsequent action potential. For each of the seven Markov conductance models, I_{DynC} was measured during the interspike interval (3 ms prior to the threshold potential of the subsequent action potential), and the mean I_{DynC} was calculated for each model. Across the seven Markov models, these mean I_{DynC} values were plotted against the mean percent increase in repetitive firing (Figure 6B) for each model. This plot revealed a strong positive correlation ($r^2 = 0.93$), suggesting the steady-state Nav current, which occurs at subthreshold voltages, is a critical parameter for Nav conductance mediated increases in repetitive firing frequency. In contrast, if the I_{DynC} value was measured at the peak of the action potential waveform (see Figure 6A schematic), there was no correlation ($r^2 = 0.004$) with the ability of each model to increase repetitive firing frequency (Figure 6C).

To examine more directly how each current component affected firing, we plotted the peak I_{NaT}, I_{NaR}, and I_{NaP} values from each model (as it was measured at a single voltage-step), against the mean increase in repetitive firing frequency after the model was applied in dynamic clamp. Again, these plots reveal a strong correlation between I_{NaP} measured at -65 mV and the change in repetitive firing rate (Figure 6D), while I_{NaR} (Figure 6E), and I_{NaT} (Figure 6F) values were not significantly correlated to the mean increases in repetitive firing rate.

Markov model open state occupancy indicates steady-state I_{NaP} is the primary depolarizing drive of subsequent action potentials

Across models, we hoped to determine why scaling peak I_{NaR} does not affect the repetitive firing properties of Purkinje neurons. To analyze this more directly, we used voltage-clamp simulation experiments in which the voltage command consisted of two consecutive action potential waveforms previously recorded from a Purkinje neuron firing at ~60 Hz. Under this voltage-clamp paradigm, we analyzed the performance of the nominal model in addition to the 'I_{NaR} reduced' model (orange), and the 'I_{NaP} reduced model' (red) presented in Figure 4. In addition to examining the current evoked by this voltage command for each model, we measured and plotted occupancy in the open/conducting kinetic state. Time-locked traces from this examination are presented in Figure 7. In comparing the 'I_{NaR} reduced' model (*orange*) traces with the nominal (*black*) traces, there was only a slight difference in the open-state occupancy (middle traces) and evoked steady-state I_{Na} traces during the interspike interval. This is consistent with the 'I_{NaR} reduced' model having only a slightly smaller I_{NaP} component than the nominal model (see Figure 4A2). From the current traces presented in Figure 7, we found no evidence for reduced I_{NaR} in the 'I_{NaR} reduced model' current or open-state occupancy traces. This is likely because I_{NaR} is very small at these subthreshold voltages and because the decay of I_{NaR} is relatively rapid at hyperpolarized membrane potentials. However, the 'I_{NaP} reduced' model (*red traces*) has significantly less open-state-occupancy corresponding to less steady-state evoked I_{Na} during the interspike interval, revealing why the 'I_{NaP} reduced' model, when applied using dynamic clamp, results in significantly lower firing frequencies than the nominal model and the 'I_{NaR} reduced' model (see Figure 4C).

Peak I_{NaP} and I_{NaR} can be inversely adjusted by adjusting occupancy in the slow inactivated kinetic state

In developing the various models with alterations in I_{NaP} and I_{NaR}, it became evident that increased occupancy in the slow inactivated kinetic state, shown as IS in the Markov kinetic state models (Figure 8A), was necessary to increase peak I_{NaR}. On reflection, this is unsurprising because the decay of the I_{NaR} current is simulated in these Markov models by transiting open channels into the IS state. Any simulated channels that fail to transit from the open state into IS should then contribute to I_{NaP}. According to these model properties, we reasoned that we should be able to inversely scale peak I_{NaP} and I_{NaR} by adjusting the rate constants that affect Open and IS occupancy. These rate constants are labeled b2s and a2s and are highlighted in panel 8A. We conducted voltage-clamp simulation studies to test this hypothesis and indeed found that reducing the b2s rate constant results in an increase in the proportion of I_{NaR} and reduces I_{NaP} (Figure 8B). Alternatively, if the a2s rate constant is reduced, peak I_{NaP} is increased and I_{NaR} is diminished. As current traces in Figure 8B traces reveal, inversely adjusting I_{NaR} and I_{NaP} in this way does not affect recovery of fast-inactivated channels into the open state, i.e., channels are still able to recover from fast-inactivation into an open/conducting state on repolarization of the membrane.

Previous dynamic clamp experiments suggest peak I_{NaR} has no significant impact on the firing rate or action potential waveform properties of cerebellar Purkinje neurons. However, in adjusting rate constants that affect occupancy in the slow inactivated state, we inversely scale I_{NaR} and I_{NaP}. These data indicate the presence of I_{NaR} may reflect the degree of Nav channel slow inactivation, which could regulate or fine-tune the population of Nav channels available to participate in I_{NaP}. We hypothesized that adjusting slow inactivation occupancy, and increasing or decreasing I_{NaP}, as we have done if Figure 8B, will result in increased or decreased repetitive firing rates. To test this hypothesis, we applied the models developed in Figure 8B in dynamic clamp experiments, using application of the nominal model in dynamic clamp as a baseline. Indeed, as panels 8C and 8D show, adjusting the transiting of open channels into the IS state can be used to inversely scale I_{NaR} and I_{NaP}, which results in significant (compared to the nominal model) increases or decreases in both spontaneous (Fig. 8C) and evoked (Fig. 8D) repetitive firing frequencies.

Discussion

We used dynamic clamp to apply several Nav conductance models, which have varying resurgent (I_{NaR}) and persistent (I_{NaP}) Nav current properties, to test how these current components contribute to the firing of adult cerebellar Purkinje neurons. Results from these experiments indicate peak I_{NaR} does not directly contribute to the repetitive firing rates of Purkinje neurons. Instead, the amplitude of I_{NaP}, particularly at subthreshold voltages, reliably scales firing frequency regardless of I_{NaR} amplitude. These studies also revealed I_{NaR} and I_{NaP} can be inversely scaled by adjusting occupancy in the slow inactivated kinetic state, whereby slow inactivation removes Nav channels from contributing to I_{NaP}.

I_{NaR} and excitability

In our initial experiments, we constructed two Markov kinetic state models with decreased or increased I_{NaR} by adjusting the properties of two pairs of state transition rate constants of a previously developed Nav conductance model (Ransdell et al., 2022). These hand-tuned model conductances were applied in dynamic clamp experiments and the effects of each conductance on action potential firing were assessed. Surprisingly, after adding a model Nav conductance with an increased I_{NaR} component, there were no significant changes in firing frequency compared to the base (nominal) model (Figure 2). Additional dynamic clamp studies utilized Nav models which differ in the peak amplitude of I_{NaR} and I_{NaP}, or that vary in the time constant of I_{NaR} decay. These studies revealed I_{NaP} is the critical Nav conductance parameter for tuning Purkinje neuron repetitive firing frequency, while peak I_{NaR} has no effect on firing frequency or the action potential waveform. Of course, this provokes an important question- what role does I_{NaR} serve in regulating Purkinje neuron function if it has no effect on action potential firing? We propose I_{NaR}, or more specifically the decay of I_{NaR} (which is rapid at subthreshold voltages), may reflect the removal of non-inactivating Nav channels into a slow inactivated kinetic state, and thus, I_{NaR} reflects a mechanism by which Purkinje neuron I_{NaP} is regulated.

There is a long-standing hypothesis that I_{NaR} increases membrane excitability and scales neuronal repetitive firing rates since its discovery by Raman and Bean in 1997. *Scn8a* mutant mice (*Scn8a* null) have reduced I_{NaR} (by 90%) and reduced Purkinje neuron firing frequencies, which suggests I_{NaR} contributes to repetitive action potential generation (Raman et al., 1997). However, it was also noted that the targeted deletion of *Scn8a* results in reduced (by ~70%) I_{NaP}, which may have caused the attenuated repetitive firing rates (see Figures 4, 8). *Scn8a* null mice were also found

to have hyperpolarized interspike voltages, which also might reflect attenuated subthreshold I_{NaP} (Raman et al., 1997).

The decay of I_{NaR} at subthreshold voltages is rapid (~3 ms) (Raman and Bean, 1997), suggesting the majority of depolarizing Nav current during interspike intervals, and the Nav current immediately preceding action potentials during repetitive firing, is a result of subthreshold I_{NaP}. Subthreshold Nav current has previously been shown to play a critical role in setting the rate of interspike interval depolarization as well as the action potential threshold voltage in mouse Purkinje neurons as well as CA1 hippocampal neurons (Carter et al., 2012). The Markov conductance models developed here and dynamic clamp studies presented in Figure 3 reveal that even if the tau of I_{NaR} decay is increased (nearly doubled at -65 mV) or decreased, compared to the nominal model (Figure 3B), the effects of I_{NaR} on repetitive firing are similar (Figure 3E), revealing I_{NaR} does not directly influence repetitive firing frequency even with much slower decay kinetics (see Figure 3).

Targeted deletion of *Scn4b*, which encodes the Nav channel β4 (Navβ4) subunit, results in reduced firing rates, as well as reduced (by ~50%) peak I_{NaR} in Purkinje neurons (Ransdell et al., 2017). Importantly, this result was consistent with an earlier study which found the deletion of *Scn4b* causes reduced I_{NaR} and evoked firing rates in rat striatal medium spiny neurons (Miyazaki et al., 2014). To test if the deficits in *Scn4b*$^{-/-}$ Purkinje neuron firing could be rescued, Ransdell et al. (2017) applied a modeled I_{NaR} conductance via dynamic clamp to these cells and found that finding firing rates could be rescued to wild type levels (Ransdell et al., 2017) with the additional Nav conductance. Importantly, the model Nav conductance utilized in Ransdell et al., (2017) included a persistent Nav component. The effect of targeted *Scn4b* deletion on I_{NaP} was not investigated in this study. In RA projection neurons (RAPNs) of the adult zebra finch, Zemel and colleagues present a collection of data showing that RAPN maturation includes paired increases in repetitive firing frequency and peak I_{NaR}, which corresponded with increased levels of Navβ4 expression (Zemel et al., 2021). In these studies, dynamic clamp was also used to test the role of I_{NaR} on RAPN firing frequencies, however, the I_{NaR} model used included a steady-state or persistent Nav current component. Zemel and colleagues also show adult zebra finch RAPNs have similar I_{NaR} decay kinetics as mouse Purkinje neurons (Raman and Bean, 1997), with a very short decay time constant (~2 ms) at subthreshold voltages (Zemel et al., 2021).

It was surprising that scaling the amount of I_{NaR} across conductance models did not drive consistent changes in action potential duration (Supplemental Figure 3). However, previous work has shown Purkinje neurons express large and fast-activating voltage-gated potassium currents which quickly repolarize the membrane during the action potential downstroke (Raman & Bean, 1999). These large hyperpolarizing conductances likely shunt I_{NaR} depolarization and prevent any consistent effect of I_{NaR} on action potential duration in Purkinje neurons. This point underscores the reasonable assumption that the roles of I_{NaR} in regulating membrane excitability will vary across neuronal cell types with unique firing and ion channel expression properties (Lewis & Raman, 2014).

Persistent current and its relationship with resurgent current

Since the discovery of the non-inactivating/persistent sodium current in Purkinje neurons (Llinás & Sugimori, 1980), I_{NaP} has been implicated in promoting repetitive and complex firing in several neuronal cell types (Carter et al., 2012; Han et al., 2015; Lee & Heckman, 2001; Taddese & Bean, 2002; Yamanishi et al., 2018). Experiments here demonstrate the amplitude of I_{NaP} is critical for

regulating the firing frequency of Purkinje neurons (Figure 6D), and that I_{NaR} may reflect an important mechanism by which Nav channels are removed from contributing to I_{NaP}. Increased levels of I_{NaP} and I_{NaR} have often been identified as a result of gain-of-function mutations in Nav channel α subunits which are associated with human diseases such as paroxysmal extreme pain disorder (PEPD), long QT syndrome, and epilepsies (Eberhardt et al., 2014; Hargus et al., 2013; Jarecki et al., 2010; Pan & Cummins, 2020). Jarecki and colleagues (2010) transfected cultured DRG neurons with mutant Nav1.7, Nav1.5, and Nav1.4 channels associated with PEPD, long-QT3 syndrome, and paramyotonia congenita, respectively, and found these mutations caused dual increases in both I_{NaR} and I_{NaP}. Similarly, heterologously expressed human mutant Nav1.7 channels, associated with overlapping inherited erythromelagia and PEPD symptoms, was found to produce increased peak I_{NaR} and I_{NaP} as well as reduced Nav channel slow inactivation compared to wild type Nav1.7 (Eberhardt et al., 2014; Estacion et al., 2008). In cultured ND7/23 cells, several Scn8a mutations linked with early infantile epileptic encephalopathy were also found to increase I_{NaR} and I_{NaP} (Pan & Cummins, 2020). Similarly, medial entorhinal cortex layer II neurons were found to have increased I_{NaR} and I_{NaP} in mice after induced epileptogenesis and before onset of seizures (Hargus et al., 2013). In addition to the increased levels of I_{NaR} and I_{NaP}, several of the cells in these studies were found to have increased action potential firing (Estacion et al., 2008; Hargus et al., 2013; Pan & Cummins, 2020). Mutations in Nav channel pore-forming α subunits, which drive singular or dual changes in I_{NaR} and/or I_{NaP}, provide important details regarding how changes in Nav channel activation, fast-inactivation, and slow-inactivation processes affect these current components, and additionally, how alterations in I_{NaR} and/or I_{NaP} affect membrane excitability. For instance, PEPD-associated mutations in Nav1.7 typically impact the voltage-dependence of fast-inactivation resulting in enhanced I_{NaP} (Dib-Hajj et al., 2013; Eberhardt et al., 2014). It will be interesting, and directly relevant to the results presented here, to examine how mutations in Nav channel pore-forming or accessory subunits affect I_{NaR} and I_{NaP} along with Nav channel slow inactivation processes in native neuronal cell types. The expression of Nav channel pore-forming α subunits, even in the presence of an Nav channel accessory subunit such as Navβ4, is not sufficient reconstitute I_{NaR} in heterologous expression systems (Aman et al., 2009; Chen et al., 2008; Theile et al., 2011). I_{NaR} is typically measured in heterologous cells by expressing a select Nav channel α subunit and applying, via the patch electrode, a 14-residue synthetic peptide homologous to cytoplasmic tail of Navβ4 (Lewis & Raman, 2011), which may distort how a given Nav channel mutation affects I_{NaR} properties. A recent study, however, was successful in reconstituting I_{NaR} in heterologous cells by expressing an Nav channel α subunit (Nav1.8 or Nav1.9) along with the A-type splice variant of intracellular fibroblast growth factors (Xiao et al., 2022).

Slow inactivation and adjusting the ratio of I_{NaR} and I_{NaP}

I_{NaR} decay is proposed to reflect the transiting of Nav channels from an open/activated state into a slow inactivated kinetic state (Ransdell et al., 2022). Nav channel slow inactivation is distinct from conventional fast-inactivation and occurs during prolonged periods of Nav channel activation, generally tens to hundreds of milliseconds (Aman & Raman, 2007; Silva, 2014) or during sustained repetitive firing. The nominal model (Ransdell et al., 2022), and other Markov models used here, have parallel inactivation pathways, a fast-inactivation pathway and slow inactivation pathway, in order to accurately reproduce the fast-inactivation kinetics of I_{NaT} and slower decay of I_{NaR} at steady-state voltages (see Figures 1A, C). Adjusting rate constants that determine entry into and out of the slow inactivated kinetic state readily tunes the portion of I_{NaR} and I_{NaP}, which determines the model's effect on Purkinje neuron repetitive firing (Figure 8). By

increasing occupancy in the slow-inactivated kinetic state, I_{NaR} is increased and I_{NaP} is decreased. Alternatively, reducing occupancy in the slow inactivated kinetic state decreases I_{NaR} and increases I_{NaP}. The magnitude of I_{NaP} is directly linked to the Nav model's effect on repetitive firing rate. From these results, it seems Nav channels can be regulated in at least two domains in order to adjust repetitive firing frequency: 1. The proportion of channels that are activated and fail to inactivate at subthreshold voltages, and 2. The proportion of these non-inactivating channels which undergo slow inactivation. These domains of Nav channel regulation would regulate the level of subthreshold I_{NaP} during interspike intervals, which, as our dynamic clamp studies show, scales Purkinje neuron firing rates. Slow inactivation of Nav currents has previously been shown to be essential in the regulation of pacemaking activity in STN neurons (Do & Bean, 2003) and interspike voltage changes (Carter et al., 2012). Our results further suggest the magnitude of I_{NaP}, which contributes to repetitive firing, may be regulated by Nav channel slow inactivation in Purkinje neurons. Enhancing cAMP-dependent protein kinase and protein kinase C activity have been shown to rapidly enhance Nav channel slow inactivation in heterologously expressed Nav1.2 channels (Chen et al., 2006), suggesting post-translational regulation of Nav channels can quickly modify this inactivation pathway. Reduced extracellular Na^+ concentrations have also been found to increase entry into the slow inactivated kinetic state (Afshari et al., 2004; Aman & Raman, 2007; Townsend & Horn, 1997), although it's not known if this mechanism of regulation functions in a physiological context. Moving forward, it will be interesting to test how the regulation of slow inactivation processes in native neuronal cell types affect individual Nav current components, particularly I_{NaR} and I_{NaP}, and to determine if post-translational regulation of Nav channel slow inactivation is capable/necessary for the fine-tuning of I_{NaP} as well as firing rates in spontaneously active cells.

Figure Legends

Figure 1. Dynamic clamp addition of a modeled Nav conductance increases the spontaneous firing frequency of adult cerebellar Purkinje neurons **A.** Voltage clamp step protocol (top) and current traces of the evoked fast-transient (I_{NaT}) and resurgent (I_{NaR}) Nav currents in an acutely dissociated Purkinje neuron (*middle*). The same voltage protocol was used to evoke and measure Nav currents generated by a Markov Nav conductance model. **B.** This simulated Nav current was generated by a nine-state gating Markov matrix that includes three closed states (C1, C2, C3), two inactivated-closed states (IC1, IC2), two fast inactivated states (IF1, IF2), a slow inactivated state (IS), and an open state (O). Transition rate constant values are denoted by variables between states (see Methods). Panel **C.** shows a schematic of the dynamic clamp setup used to interface Nav conductance models with a current injection electrode that is patched on an adult Purkinje neuron in a sagittal brain section. A computer running SutterPatch acquisition and dynamic clamp software is interfaced with a Sutter digidata/amplifier, which is connected to the patch electrode. The computer running SutterPatch software uses voltage signals measured in the Purkinje neuron to calculate, in real-time (via the Nav conductance model) current injection values. Current injections representing the model Nav conductance are then applied to the patched cell. **D.** Spontaneous action potentials recorded from an adult Purkinje neuron before and after (**D1**) the dynamic clamp-mediated addition of the Nav conductance represented in panel B. Dynamic clamp-mediated current injections are shown in red. **D2.** Shows an expanded time trace of a single action potential (*black*) and its corresponding dynamic clamp current injection (*red*). **E.** Firing frequency of adult Purkinje neurons (*open circles*) was significantly ($P < 0.0001$, paired Student's t-test, $n = 30$) increased after dynamic clamp-mediated addition of the nominal Nav conductance (*closed circles*).

Figure 2. Adjusting peak I_{NaR} does not scale the repetitive firing frequency of Purkinje neurons **A.** To generate the 'I_{NaR} decreased' and 'I_{NaR} increased' models, transition rate constant values b2 (*green box*) and b3s (*red box*) were selectively adjusted. Values of the nominal and manipulated state transition variables at -45 mV are listed below the matrix. **B.** A simulated voltage clamp recording of evoked I_{NaR} (at -45 mV) is shown for the nominal model (black), the 'I_{NaR} increased' model (*green*), and the 'I_{NaR} decreased' model (*red*). **C.** Peak I_{NaR} values were measured at various repolarizing voltage steps after a 5 ms depolarization step to 0 mV. These peak current values are plotted against voltage for the nominal model (black), 'I_{NaR} increased' model (*green*), and the 'I_{NaR} decreased' model (*red*). I_{NaP} is digitally subtracted prior to all peak I_{NaR} measurements. All models assessed using a 400 nS conductance (see Methods). **D.** Spontaneous firing frequency of adult Purkinje neurons after dynamic clamp-mediated addition of the nominal and 'I_{NaR} decreased' model (*left, red squares*), and the nominal and 'I_{NaR} increased' model (*right, green triangles*). Spontaneous firing frequency of the 'I_{NaR} decreased' model is significantly reduced compared to spontaneous firing frequencies measured during application of the nominal model. Applying the 'I_{NaR} increased' model resulted in no significant change in firing frequency (paired Student's t-test, 'I_{NaR} decreased' vs nominal: $P = 0.0042$, $n = 13$; 'I_{NaR} increased' vs nominal: $P = 0.21$, $n = 13$).

Figure 3. Purkinje neuron repetitive firing rates are not affected by adjusting the time constant of I_{NaR} decay. An automated optimization (script) procedure utilizing the Nelder-Mead "amoeba" algorithm (Nelder and Mead, 1965; Lagarias et al., 1998) was used to apply targeted changes to Nav conductance models while preserving other aspects of the nominal Nav conductance model. A schematic of this process is shown in panel **A.** A MATLAB script was used to apply the amoeba

algorithm, checking the difference between the simulation prediction and the target experimental values with each iteration, and 'crawling' through potential rate constant values in order to minimize total error. **B.** This amoeba method was used to generate two new Markov conductance models with targeted changes in the time constant of I_{NaR} decay. The time constant of I_{NaR} decay (τdecay) is plotted against voltage for the original nominal model and the two newly generated models, 'τdecay decreased' (*green squares*) and 'τdecay increased' (*blue triangles*). **C.** A simulated voltage clamp recording of model generating I_{NaR} is shown for the nominal (*black*), 'τdecay decreased' (*green*), and 'τdecay increased' (*blue*) models. **C1.** For each model, peak I_{NaR} values are normalized to the max I_{NaR} generated by the nominal model and are plotted against voltage. Similar plots of normalized I_{NaP} and I_{NaT} are presented in panels **C2.** and **C3.**, respectively. **D.** Representative traces showing dynamic clamp-mediated addition of the 'τdecay reduced' (*green*) and 'τdecay increased' (*blue*) conductances in the same cell. Voltage records are shown in black with the corresponding dynamic clamp current injections shown below. **E.** Spontaneous firing frequencies measured in Purkinje neurons after the addition of the nominal (*black circles*), 'τdecay decreased' (*green squares*), and 'τdecay increased' (*blue triangles*) model conductances (400 nS) are plotted with lines connecting measurements taken from the same cell. Adding the 'τdecay decreased' and the 'τdecay increased' model conductances resulted in spontaneous firing frequencies that were significantly reduced compared to firing frequencies measured after adding the nominal model conductance, however, the addition of 'τdecay decreased' and the 'τdecay increased' model conductances resulted in similar repetitive firing frequencies (paired Student's t-test- τdecay decreased vs nominal, $P < 0.0001$, $n = 29$; τdecay increased vs nominal, $P < 0.0001$, $n = 29$; τdecay increased vs τdecay decreased, $P = 0.94$, $n = 29$).

Figure 4. Reducing the amount of I_{NaP} modeled conductance significantly decreases spontaneous firing frequency compared to the nominal model, while reducing I_{NaR} does not. **A.** Voltage clamp simulation traces showing Nav currents generated by the nominal (*black*), 'I_{NaP} reduced' (*red*), and 'I_{NaR} reduced' (*orange*) models are shown with the common voltage command shown above. **A1-A3.** Peak I_{NaR} (A1), I_{NaP} (A2), and I_{NaT} (A3) were normalized to the peak Nav currents generated by the nominal model and are plotted against voltage. **B.** Representative action potential firing during dynamic clamp-mediated addition of the 'I_{NaR} reduced' (*upper*) or 'I_{NaP} reduced' (*lower*) conductance models is shown from the same Purkinje neuron. Dynamic clamp current injections are presented as orange or red traces. **C.** The spontaneous firing frequency of Purkinje neurons with addition of the nominal (*black circles*) conductance model was not significantly changed after addition of the 'I_{NaR} reduced' conductance model (*left, orange triangles*). However, this firing frequency was significantly decreased after the addition of the 'I_{NaP} reduced' conductance model (*right, red diamonds*). (Paired Student's t-test. nominal vs 'I_{NaR} reduced', $P = 0.21$, $n = 29$; nominal vs 'I_{NaP} reduced', $P < 0.0001$, $n = 29$).

Figure 5. Applying or subtracting an isolated I_{NaP} conductance scales repetitive firing in Purkinje neurons **A.** A Hodgkin-Huxley (HH) modeled conductance (using 3.4 nS conductance) was used to simulate isolated I_{NaP}. The current traces presented in panel A. show simulated voltage clamp of this modeled conductance. **B.** Simulated peak I_{NaP} values versus voltage steps generated by the nominal conductance model (*black*, 400 nS) are compared directly to the HH model (*blue*, 3.4 nS). The HH model's conductance values were adjusted so that peak I_{NaP} measurements would match the peak I_{NaP} generated by 400 nS of the nominal model. An example of applying the HH model in dynamic clamp experiments is shown to the right; the dynamic clamp current injection is presented in blue. **C.** Spontaneous firing frequency of Purkinje neurons with no dynamic clamp (*open circles*) was significantly increased after dynamic clamp addition of 3.4 nS of the HH

conductance model (*left, blue squares*) and significantly decreased after addition of -3.4 nS of the HH conductance model (*right, red triangles*) (Paired Student's t-test. no model vs 3.4 nS, P = 0.0009, n = 13; no model vs -3.4 nS, P = 0.047, n = 14). **D.** The percent increase in repetitive firing frequency after addition (*left*, 3.4 nS) or subtraction (*right*, -3.4 nS) of the HH conductance model is plotted against the amplitude of dynamic clamp current injected during the interspike interval (see Methods) (3.4 nS, $r^2 = 0.68$, n = 16; -3.4 nS, $r^2 = 0.36$, n = 15).

Figure 6. Across models used for dynamic clamp, I_{NaP} is positively correlated with the changes in repetitive firing frequency. The action potential waveform shown in panel **A.** depicts how dynamic clamp current measurements were obtained. For interspike values, dynamic clamp current was recorded 3 ms before action potential threshold was reached. Note that the arrow that points to steady-state voltage is not to scale, and the measurement was not taken at this point. For peak values, dynamic clamp current was recorded during the peak (max voltage) of the action potential. **B.** A strong correlation exists between the percent increase in spontaneous firing frequency, driven by the addition of each Markov conductance model, and the dynamic clamp current injection during the interspike interval of an action potential ($r^2 = 0.93$). If the dynamic clamp current injection is measured during the peak of the action potential, the correlation coefficient (r^2) falls to 0.0035 (**C.**). **D.** The correlation between the percent increase in spontaneous firing frequency after addition of each Markov conductance model and the peak I_{NaP} (measured using voltage clamp at a -65 mV voltage step, is also strong ($r^2 = .96$; P = 0.0012,), while this positive correlation is absent if measurements of I_{NaR} (at -45 mV) (**E.**) or I_{NaT} (at 0 mV) (**F.**) are used ($r^2 = 0.41$, P = 0.12; $r^2 = 0.38$, P = 0.77, respectively). Pearson's correlation test was used to determine significance.

Figure 7. Action potential clamp experiments were conducted using a voltage command (dashed trace, *upper*) that includes two action potentials that were originally recorded from a Purkinje neuron firing at ~60 Hz. The nominal (*shown in black*), 'I_{NaR} reduced' (*shown in orange*), and 'I_{NaP} reduced' (*shown in red*) Markov conductance models (see Figure 4) were applied to a Sutter Model cell during these simulated action potential clamp experiments. Kinetic state occupancy plots, showing occupancy in the open state, are shown below (*middle traces*) and are time-locked with the voltage command. The bottom traces show the time-locked evoked currents produced by the voltage command for each of these models.

Figure 8. Peak I_{NaP} and I_{NaR} can be inversely adjusted by changing rate constants responsible for slow inactivation occupancy **A.** To develop models with inversely scaled I_{NaP} and I_{NaR}, the state transition rate constants between the open (O) and slow inactivated (IS) states were individually altered. Decreasing the b2s (*blue box*) transition rate constant (in the nominal model) resulted in a conductance model with increased I_{NaR} and decreased I_{NaP}. Decreasing the a2s (*red box*) transition rate constant resulted in a conductance model with decreased I_{NaR} and increased I_{NaP}. These changes resulted in the simulated voltage clamp traces that elicit the b2s reduced (*blue*) and a2s reduced (red) models, which are compared to the nominal model (*black*) in panel **B. C.** When compared to the nominal conductance model (black circles), spontaneous firing frequency of adult Purkinje neurons was significantly *increased* after addition of the a2s reduced model (*red squares, left*), and significantly *decreased* after addition of the b2s reduced model (*blue triangles, right*) (Paired Student's t-test. 400 nS a2s reduced, P = 0.0004, n = 8; b2s reduced, P = 0.0029, n = 9;). **D.** Representative recordings of action potentials during addition of the nominal model (*black, top*), and the a2s decreased (*red, middle*), and b2s decreased (*blue, bottom*) models (*left*) reveal scaling in spontaneous firing rates of a single Purkinje neuron. The effects of adding these models via dynamic clamp are similar in evoked firing frequency measurements, with addition of the a2s decreased model increasing evoked firing (*red*), and addition of the b2s decreased model

reducing evoked firing frequencies (*blue*), relative to evoked firing frequencies after addition of the nominal model.

Table 1. Table of rate constants for the Nominal, τdecay decreased, τdecay increased, I_{NaR} reduced, and I_{NaP} reduced Markov models. Transition rate equations are to the right of the table.

Table 2. Table of single action potential properties for the Nominal, τdecay decreased, τdecay increased, I_{NaR} reduced, and I_{NaP} reduced Markov models. The table includes the mean of each property, its standard deviation of the mean, and the p-value for the paired Student's t-test that compares an action potential with no addition of dynamic clamp that preceded it (see Methods).

Supplemental Figure 1. Frequency-current relationship for Purkinje neurons with no dynamic clamp (open circles; n = 24) and after application of all Markov models (nominal, *black circles*, n = 24; τdecay decreased, *green squares*, n = 31; τdecay increased, *blue triangles*, n = 33; I_{NaR} reduced, *orange triangles*, n = 34; I_{NaP} reduced, *red diamonds*, n = 34; I_{NaR} reduced (hand-tuned), *open grey circles*, n = 10; I_{NaR} increased (hand-tuned), *open squares*, n = 9).

Supplemental Figure 2. Spontaneous firing frequency increases after addition of all Markov models. For all comparisons a paired Student's t-test was used, and no dynamic clamp addition is represented by open circles. Spontaneous firing frequency was compared against the Nominal (*black circles*; $P < 0.0001$, n = 30) (**A.**), I_{NaP} reduced (*red diamonds*; $P < 0.0001$, n = 36) (**B.**), τdecay increased (*blue triangles*; $P < 0.0001$, n = 36) (**C.**), τdecay decreased (*green squares*; $P < 0.0001$, n = 35) (**D.**), I_{NaR} reduced (*orange triangles*; $P < 0.0001$, n = 37) (**E.**), I_{NaR} increased (hand-tuned) (*open squares*; $P < 0.0001$, n = 16) (**F.**), and I_{NaR} reduced (hand-tuned) (*grey open circles*; P = 0.0001, n = 18) (**G.**) models.

Supplemental Figure 3. Correlation between the difference of action potential threshold, duration, peak, amplitude, afterhyperpolarization, and max dv/dt before and after addition of dynamic clamp models and the peak simulated values of I_{NaP} at -65 mV (*left column*), I_{NaR} at -45 mV (*middle column*), and I_{NaT} at -30 mV (*right column*) for each model. Correlation coefficients (r^2) are generated by a simple linear regression. The asterisk denotes the r^2 value of a linear regression fit of the data that includes the 'I_{NaR} increased (hand-tuned)' model, while the r^2 value above is with that data point removed.

References

Afshari, F. S., Ptak, K., Khaliq, Z. M., Grieco, T. M., Slater, N. T., McCrimmon, D. R., & Raman, I. M. (2004). Resurgent Na Currents in Four Classes of Neurons of the Cerebellum. *Journal of Neurophysiology*, *92*(5), 2831–2843. https://doi.org/10.1152/jn.00261.2004

Aman, T. K., Grieco-Calub, T. M., Chen, C., Rusconi, R., Slat, E. A., Isom, L. L., & Raman, I. M. (2009). Regulation of Persistent Na Current by Interactions between β Subunits of Voltage-Gated Na Channels. *The Journal of Neuroscience*, *29*(7), 2027–2042. https://doi.org/10.1523/JNEUROSCI.4531-08.2009

Aman, T. K., & Raman, I. M. (2007). Subunit dependence of Na channel slow inactivation and open channel block in cerebellar neurons. *Biophysical Journal*, *92*(6), 1938–1951. https://doi.org/10.1529/biophysj.106.093500

Carter, B. C., Giessel, A. J., Sabatini, B. L., & Bean, B. P. (2012). Transient sodium current at subthreshold voltages: Activation by EPSP waveforms. *Neuron*, *75*(6), 1081–1093. https://doi.org/10.1016/j.neuron.2012.08.033

Chen, Y., Yu, F. H., Sharp, E. M., Beacham, D., Scheuer, T., & Catterall, W. A. (2008). Functional Properties and Differential Neuromodulation of Nav1.6 Channels. *Molecular and Cellular Neurosciences*, *38*(4), 607–615. https://doi.org/10.1016/j.mcn.2008.05.009

Chen, Y., Yu, F. H., Surmeier, D. J., Scheuer, T., & Catterall, W. A. (2006). Neuromodulation of Na+ channel slow inactivation via cAMP-dependent protein kinase and protein kinase C. *Neuron*, *49*(3), 409–420. https://doi.org/10.1016/j.neuron.2006.01.009

Dib-Hajj, S. D., Yang, Y., Black, J. A., & Waxman, S. G. (2013). The Na(V)1.7 sodium channel: From molecule to man. *Nature Reviews. Neuroscience*, *14*(1), 49–62. https://doi.org/10.1038/nrn3404

Do, M. T. H., & Bean, B. P. (2003). Subthreshold sodium currents and pacemaking of subthalamic neurons: Modulation by slow inactivation. *Neuron*, *39*(1), 109–120. https://doi.org/10.1016/s0896-6273(03)00360-x

Eberhardt, M., Nakajima, J., Klinger, A. B., Neacsu, C., Hühne, K., O'Reilly, A. O., Kist, A. M., Lampe, A. K., Fischer, K., Gibson, J., Nau, C., Winterpacht, A., & Lampert, A. (2014). Inherited pain: Sodium channel Nav1.7 A1632T mutation causes erythromelalgia due to a shift of fast inactivation. *The Journal of Biological Chemistry*, *289*(4), 1971–1980. https://doi.org/10.1074/jbc.M113.502211

Estacion, M., Dib-Hajj, S. D., Benke, P. J., Te Morsche, R. H. M., Eastman, E. M., Macala, L. J., Drenth, J. P. H., & Waxman, S. G. (2008). NaV1.7 gain-of-function mutations as a continuum: A1632E displays physiological changes associated with erythromelalgia and paroxysmal extreme pain disorder mutations and produces symptoms of both disorders. *The Journal of Neuroscience: The Official Journal of the Society for Neuroscience*, *28*(43), 11079–11088. https://doi.org/10.1523/JNEUROSCI.3443-08.2008

Han, C., Estacion, M., Huang, J., Vasylyev, D., Zhao, P., Dib-Hajj, S. D., & Waxman, S. G. (2015). Human Nav1.8: Enhanced persistent and ramp currents contribute to distinct firing properties of human DRG neurons. *Journal of Neurophysiology*, *113*(9), 3172–3185. https://doi.org/10.1152/jn.00113.2015

Hargus, N. J., Nigam, A., Bertram, E. H., & Patel, M. K. (2013). Evidence for a role of Nav1.6 in facilitating increases in neuronal hyperexcitability during epileptogenesis. *Journal of Neurophysiology*, *110*(5), 1144–1157. https://doi.org/10.1152/jn.00383.2013

Häusser, M., & Clark, B. A. (1997). Tonic synaptic inhibition modulates neuronal output pattern and spatiotemporal synaptic integration. *Neuron*, *19*(3), 665–678. https://doi.org/10.1016/s0896-6273(00)80379-7

Ito, M. (1984). *The Cerebellum and Neural Control* (1st ed.). Raven Press.

Ito, M., Yoshida, M., & Obata, K. (1964). Monosynaptic inhibition of the intracerebellar nuclei induced from the cerebellar cortex. *Experientia*, *20*(10), 575–576. https://doi.org/10.1007/BF02150304

Jarecki, B. W., Piekarz, A. D., Jackson, J. O., & Cummins, T. R. (2010). Human voltage-gated sodium channel mutations that cause inherited neuronal and muscle channelopathies increase resurgent sodium currents. *The Journal of Clinical Investigation*, *120*(1), 369–378. https://doi.org/10.1172/JCI40801

Khaliq, Z. M., Gouwens, N. W., & Raman, I. M. (2003). The contribution of resurgent sodium current to high-frequency firing in Purkinje neurons: An experimental and modeling study. *The Journal of Neuroscience: The Official Journal of the Society for Neuroscience*, *23*(12), 4899–4912. https://doi.org/10.1523/JNEUROSCI.23-12-04899.2003

Lagarias, J. C., Reeds, J. A., Wright, M. H., & Wright, P. E. (1998). Convergence Properties of the Nelder—Mead Simplex Method in Low Dimensions. *SIAM Journal on Optimization*, *9*(1), 112–147. https://doi.org/10.1137/S1052623496303470

Lee, R. H., & Heckman, C. J. (2001). Essential role of a fast persistent inward current in action potential initiation and control of rhythmic firing. *Journal of Neurophysiology*, *85*(1), 472–475. https://doi.org/10.1152/jn.2001.85.1.472

Lewis, A. H., & Raman, I. M. (2011). Cross-Species Conservation of Open-Channel Block by Na Channel β4 Peptides Reveals Structural Features Required for Resurgent Na Current. *The Journal of Neuroscience*, *31*(32), 11527–11536. https://doi.org/10.1523/JNEUROSCI.1428-11.2011

Lewis, A. H., & Raman, I. M. (2014). Resurgent current of voltage-gated Na+ channels. *The Journal of Physiology*, *592*(Pt 22), 4825–4838. https://doi.org/10.1113/jphysiol.2014.277582

Llinás, R., & Sugimori, M. (1980). Electrophysiological properties of in vitro Purkinje cell somata in mammalian cerebellar slices. *The Journal of Physiology*, *305*, 171–195. https://doi.org/10.1113/jphysiol.1980.sp013357

Miyazaki, H., Oyama, F., Inoue, R., Aosaki, T., Abe, T., Kiyonari, H., Kino, Y., Kurosawa, M., Shimizu, J., Ogiwara, I., Yamakawa, K., Koshimizu, Y., Fujiyama, F., Kaneko, T., Shimizu, H., Nagatomo, K., Yamada, K., Shimogori, T., Hattori, N., … Nukina, N. (2014). Singular localization of sodium channel β4 subunit in unmyelinated fibres and its role in the striatum. *Nature Communications*, *5*, 5525. https://doi.org/10.1038/ncomms6525

Moreno, J. D., Lewis, T. J., & Clancy, C. E. (2016). Parameterization for In-Silico Modeling of Ion Channel Interactions with Drugs. *PLOS ONE*, *11*(3), e0150761. https://doi.org/10.1371/journal.pone.0150761

Nelder, J. A., & Mead, R. (1965). A Simplex Method for Function Minimization. *The Computer Journal*, *7*(4), 308–313. https://doi.org/10.1093/comjnl/7.4.308

Obata, K., Ito, M., Ochi, R., & Sato, N. (1967). Pharmacological properties of the postsynaptic inhibition by Purkinje cell axons and the action of γ-aminobutyric acid on Deiters neurones. *Experimental Brain Research*, *4*(1), 43–57. https://doi.org/10.1007/BF00235216

Obata, K., Takeda, K., & Shtnozaki, H. (1970). Further study on pharmacological properties of the cerebellar-induced inhibition of Deiters neurones. *Experimental Brain Research*, *11*(4), 327–342. https://doi.org/10.1007/BF00237907

Pan, Y., & Cummins, T. R. (2020). Distinct functional alterations in SCN8A epilepsy mutant channels. *The Journal of Physiology*, *598*(2), 381–401. https://doi.org/10.1113/JP278952

Quattrocolo, G., Dunville, K., & Nigro, M. J. (2021). Resurgent Sodium Current in Neurons of the Cerebral Cortex. *Frontiers in Cellular Neuroscience*, *15*, 760610. https://doi.org/10.3389/fncel.2021.760610

Raman, I. M. (2023). The Hodgkin-Huxley-Katz Prize Lecture: A Markov model with permeation-dependent gating that accounts for resurgent current of voltage-gated Na channels. *The Journal of Physiology*. https://doi.org/10.1113/JP285166

Raman, I. M., & Bean, B. P. (1997). Resurgent sodium current and action potential formation in dissociated cerebellar Purkinje neurons. *The Journal of Neuroscience: The Official Journal of the Society for Neuroscience*, *17*(12), 4517–4526. https://doi.org/10.1523/JNEUROSCI.17-12-04517.1997

Raman, I. M., & Bean, B. P. (1999). Ionic currents underlying spontaneous action potentials in isolated cerebellar Purkinje neurons. *The Journal of Neuroscience: The Official Journal of the Society for Neuroscience*, *19*(5), 1663–1674. https://doi.org/10.1523/JNEUROSCI.19-05-01663.1999

Raman, I. M., Sprunger, L. K., Meisler, M. H., & Bean, B. P. (1997). Altered subthreshold sodium currents and disrupted firing patterns in Purkinje neurons of Scn8a mutant mice. *Neuron*, *19*(4), 881–891. https://doi.org/10.1016/s0896-6273(00)80969-1

Ransdell, J. L., Dranoff, E., Lau, B., Lo, W.-L., Donermeyer, D. L., Allen, P. M., & Nerbonne, J. M. (2017). Loss of Navβ4-Mediated Regulation of Sodium Currents in Adult Purkinje Neurons Disrupts Firing and Impairs Motor Coordination and Balance. *Cell Reports*, *19*(3), 532–544. https://doi.org/10.1016/j.celrep.2017.03.068

Ransdell, J. L., Moreno, J. D., Bhagavan, D., Silva, J. R., & Nerbonne, J. M. (2022). Intrinsic mechanisms in the gating of resurgent Na+ currents. *eLife*, *11*, e70173. https://doi.org/10.7554/eLife.70173

Ransdell, J. L., & Nerbonne, J. M. (2018). Voltage-gated sodium currents in cerebellar Purkinje neurons: Functional and molecular diversity. *Cellular and Molecular Life Sciences: CMLS*, *75*(19), 3495–3505. https://doi.org/10.1007/s00018-018-2868-y

Silva, J. (2014). Slow inactivation of Na(+) channels. *Handbook of Experimental Pharmacology*, *221*, 33–49. https://doi.org/10.1007/978-3-642-41588-3_3

Solinas, S., Forti, L., Cesana, E., Mapelli, J., De Schutter, E., & D'Angelo, E. (2007). Computational reconstruction of pacemaking and intrinsic electroresponsiveness in

cerebellar Golgi cells. *Frontiers in Cellular Neuroscience*, *1*, 2. https://doi.org/10.3389/neuro.03.002.2007

Taddese, A., & Bean, B. P. (2002). Subthreshold Sodium Current from Rapidly Inactivating Sodium Channels Drives Spontaneous Firing of Tuberomammillary Neurons. *Neuron*, *33*(4), 587–600. https://doi.org/10.1016/S0896-6273(02)00574-3

Thach, W. T. (1968). Discharge of Purkinje and cerebellar nuclear neurons during rapidly alternating arm movements in the monkey. *Journal of Neurophysiology*, *31*(5), 785–797. https://doi.org/10.1152/jn.1968.31.5.785

Theile, J. W., Jarecki, B. W., Piekarz, A. D., & Cummins, T. R. (2011). Nav1.7 mutations associated with paroxysmal extreme pain disorder, but not erythromelalgia, enhance Navβ4 peptide-mediated resurgent sodium currents. *The Journal of Physiology*, *589*(Pt 3), 597–608. https://doi.org/10.1113/jphysiol.2010.200915

Townsend, C., & Horn, R. (1997). Effect of alkali metal cations on slow inactivation of cardiac Na+ channels. *The Journal of General Physiology*, *110*(1), 23–33. https://doi.org/10.1085/jgp.110.1.23

Xiao, Y., Theile, J. W., Zybura, A., Pan, Y., Lin, Z., & Cummins, T. R. (2022). A-type FHFs mediate resurgent currents through TTX-resistant voltage-gated sodium channels. *eLife*, *11*, e77558. https://doi.org/10.7554/eLife.77558

Yamanishi, T., Koizumi, H., Navarro, M. A., Milescu, L. S., & Smith, J. C. (2018). Kinetic properties of persistent Na+ current orchestrate oscillatory bursting in respiratory neurons. *The Journal of General Physiology*, *150*(11), 1523–1540. https://doi.org/10.1085/jgp.201812100

Zemel, B. M., Nevue, A. A., Dagostin, A., Lovell, P. V., Mello, C. V., & von Gersdorff, H. (2021). Resurgent Na+ currents promote ultrafast spiking in projection neurons that drive fine motor control. *Nature Communications*, *12*(1), 6762. https://doi.org/10.1038/s41467-021-26521-3

909

Figure 1. Brown et al.

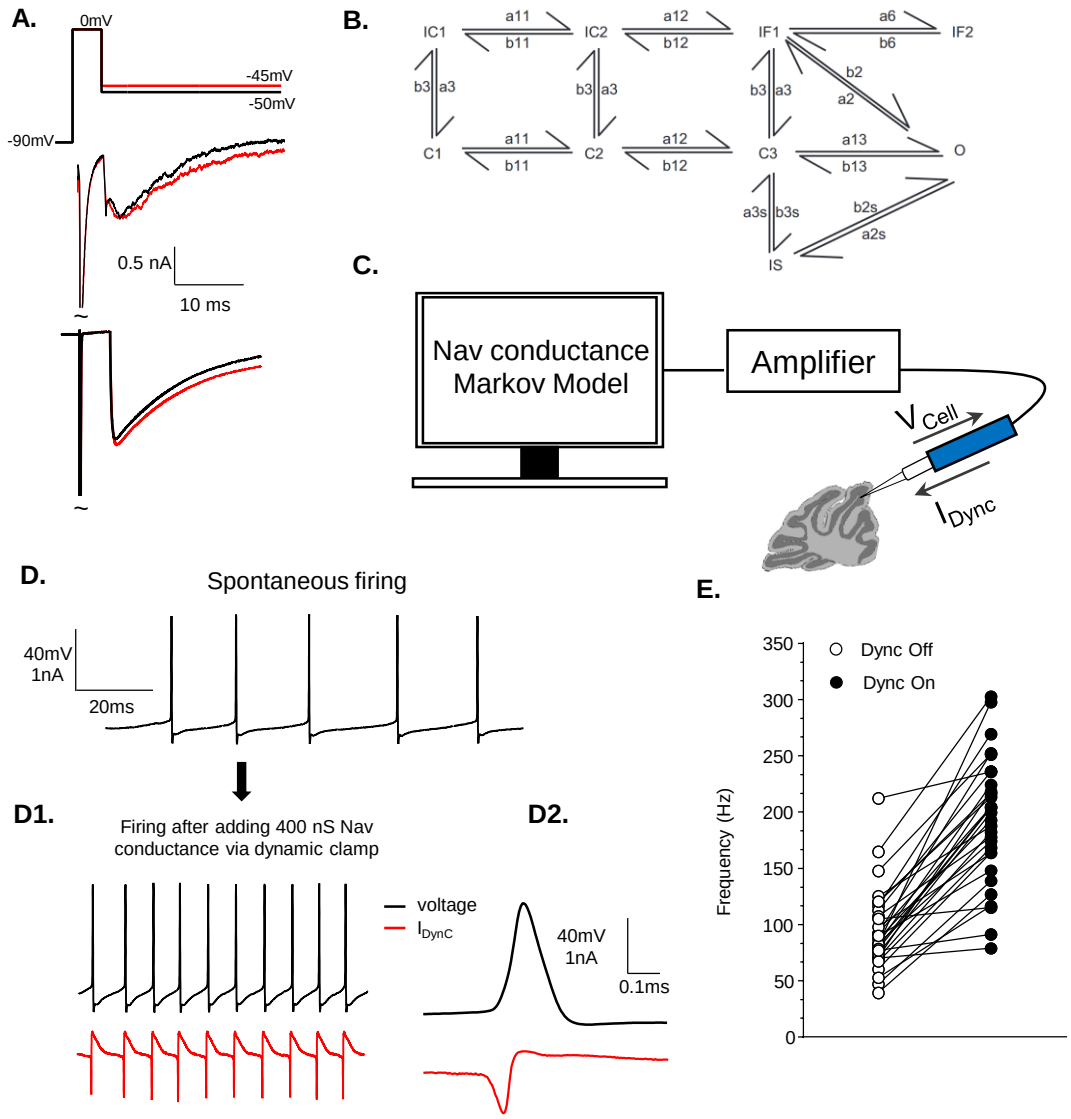

Figure 2. Brown et al.

A.

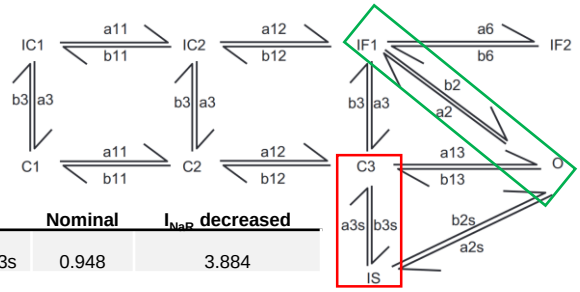

	Nominal	I_{NaR} decreased
b3s	0.948	3.884

	Nominal	I_{NaR} increased
b2	0.108	3.787

B.

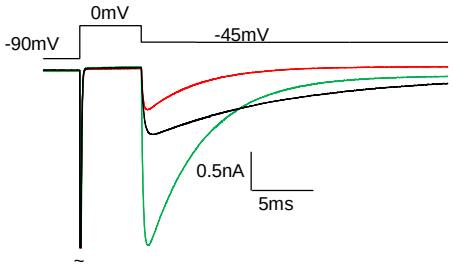

C.

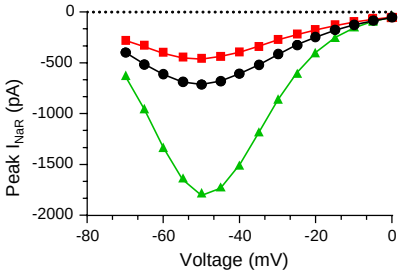

τdecay of I_{NaR}	I_{NaT} at -45mV	I_{NaP} at -45mV
11.9ms	-3531.1pA	-119.7pA
4.3ms	-2496.6pA	-27.2pA
4.5ms	-3840.5pA	-127.8pA

D.

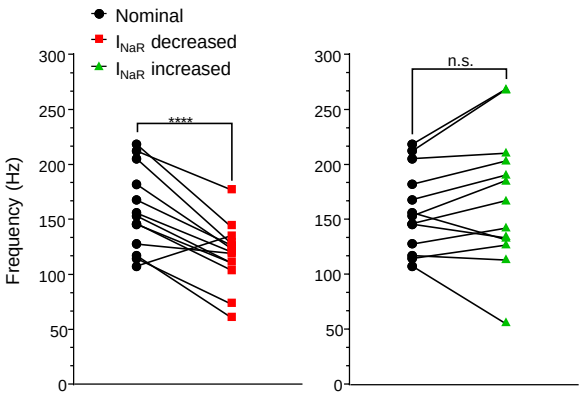

Figure 3. Brown et al.

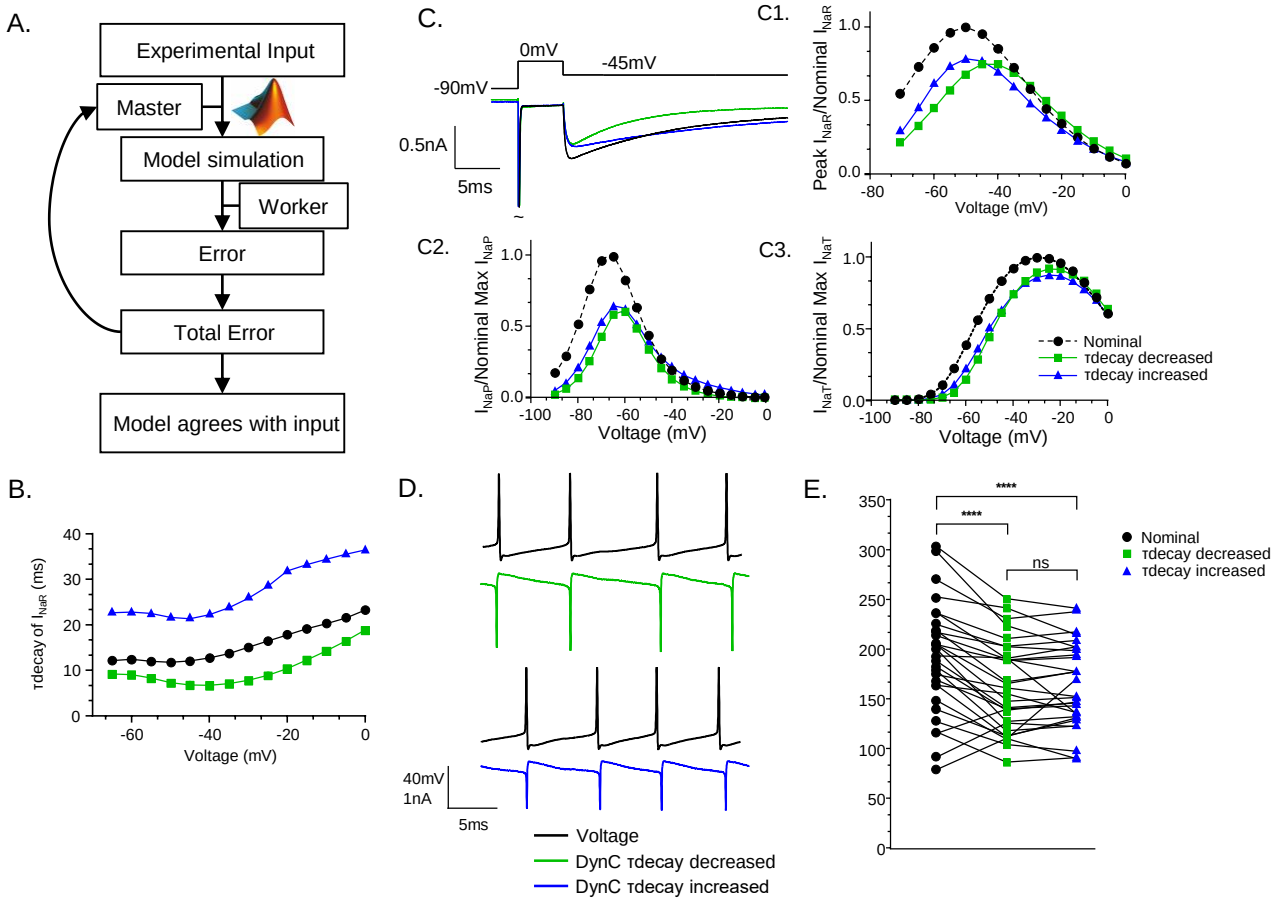

Figure 4. Brown et al.

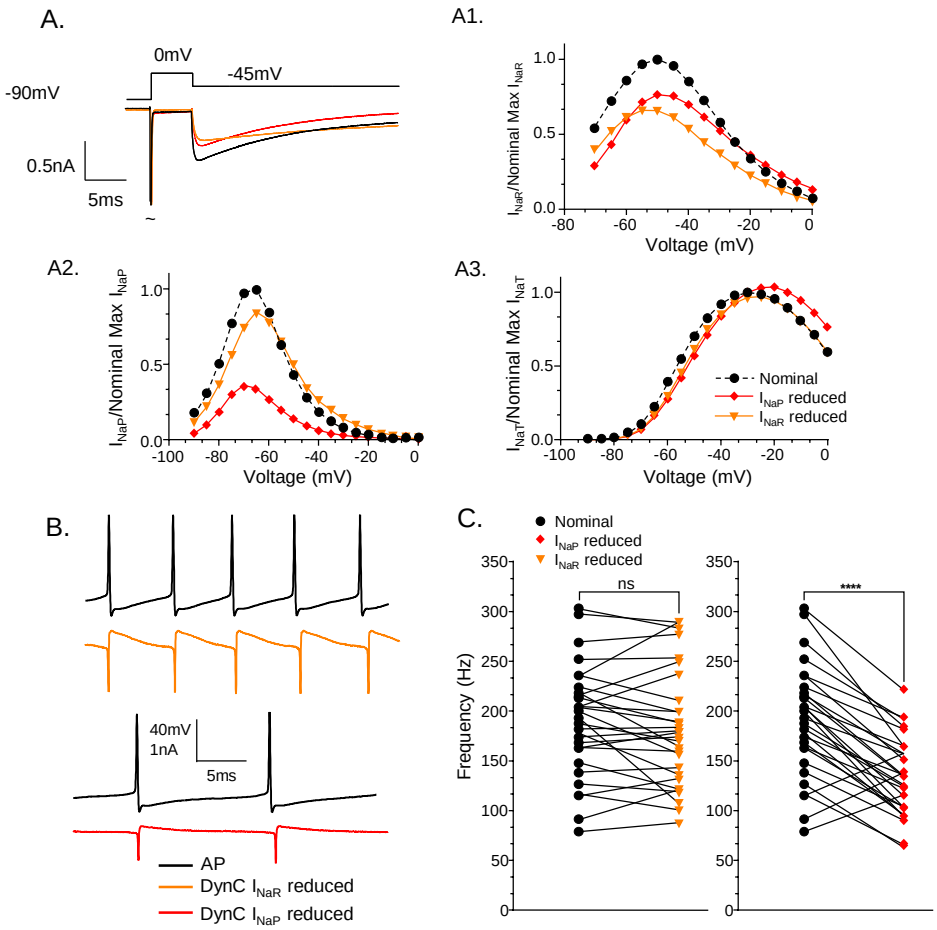

Figure 5. Brown et al.

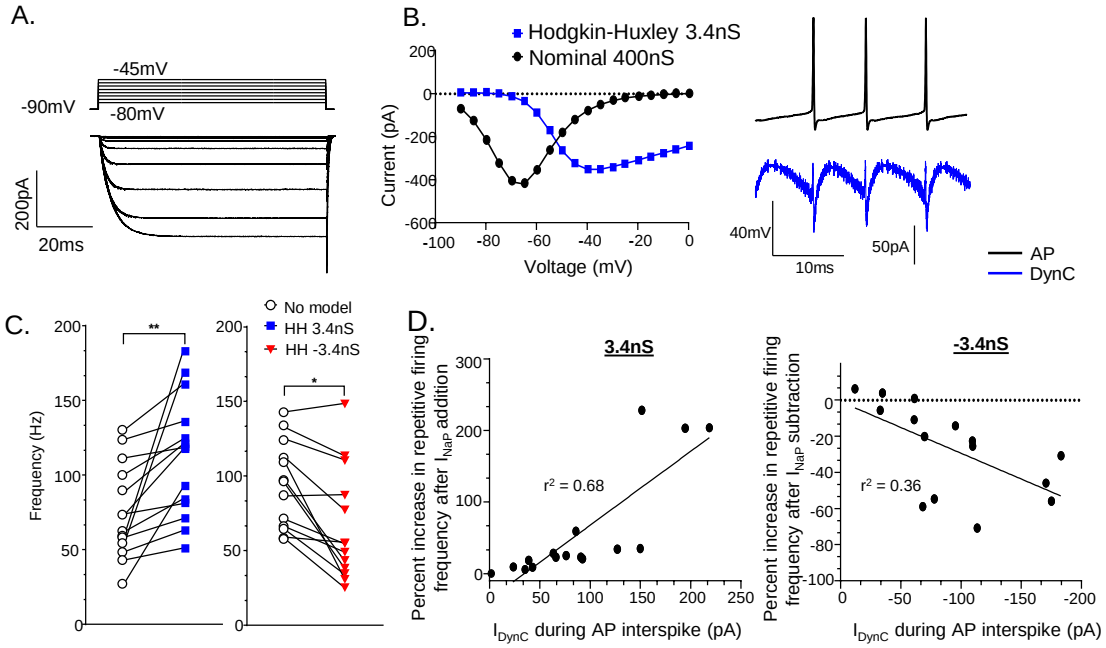

Figure 6. Brown et al.

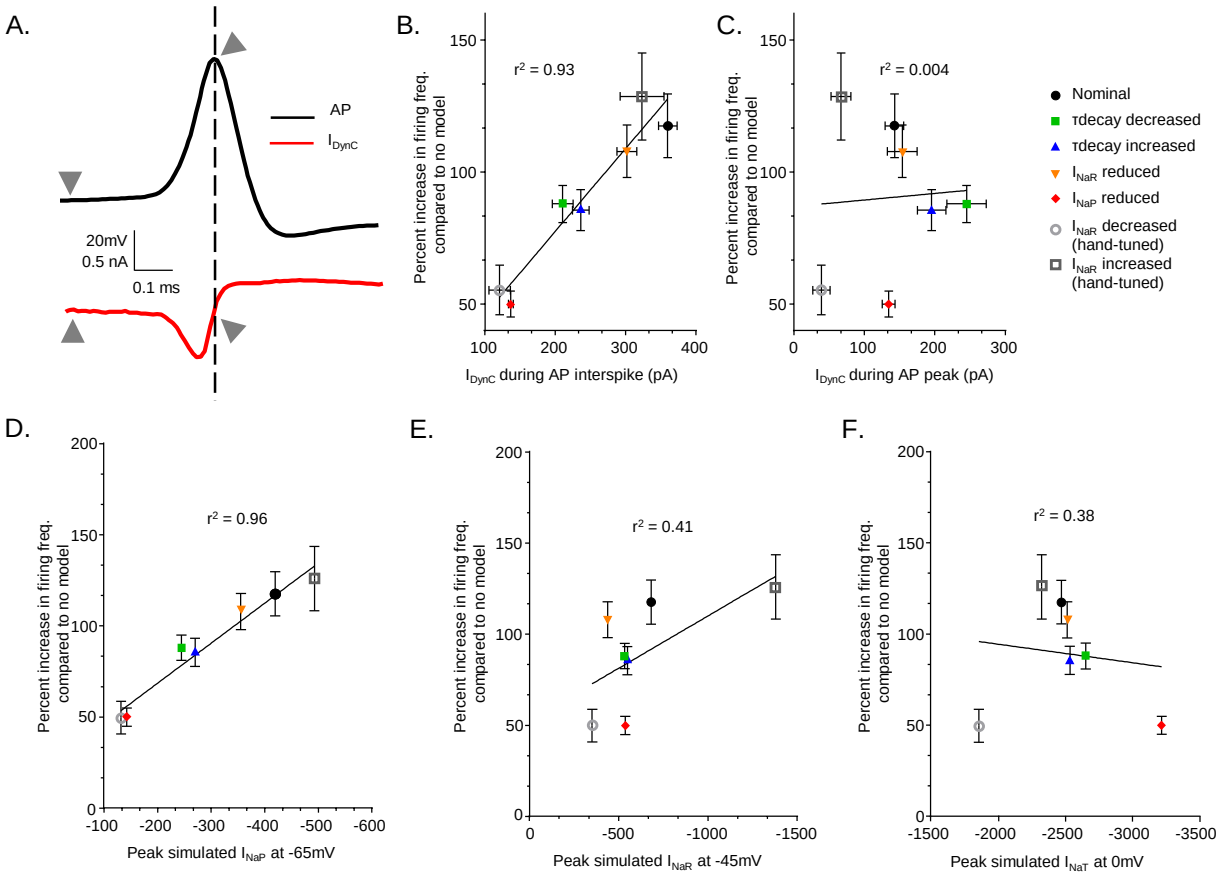

Figure 7. Brown et al.

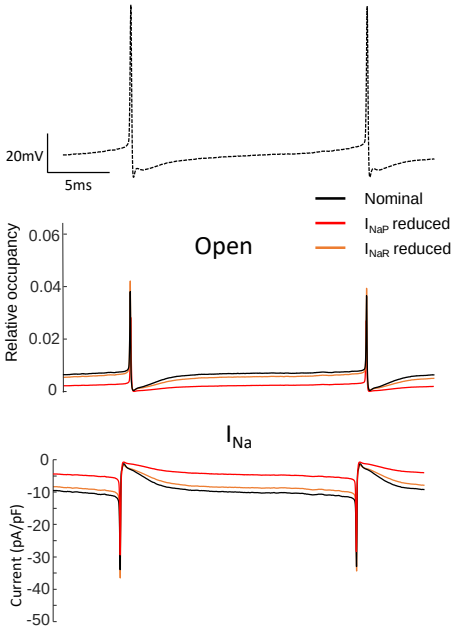

Figure 8. Brown et al.

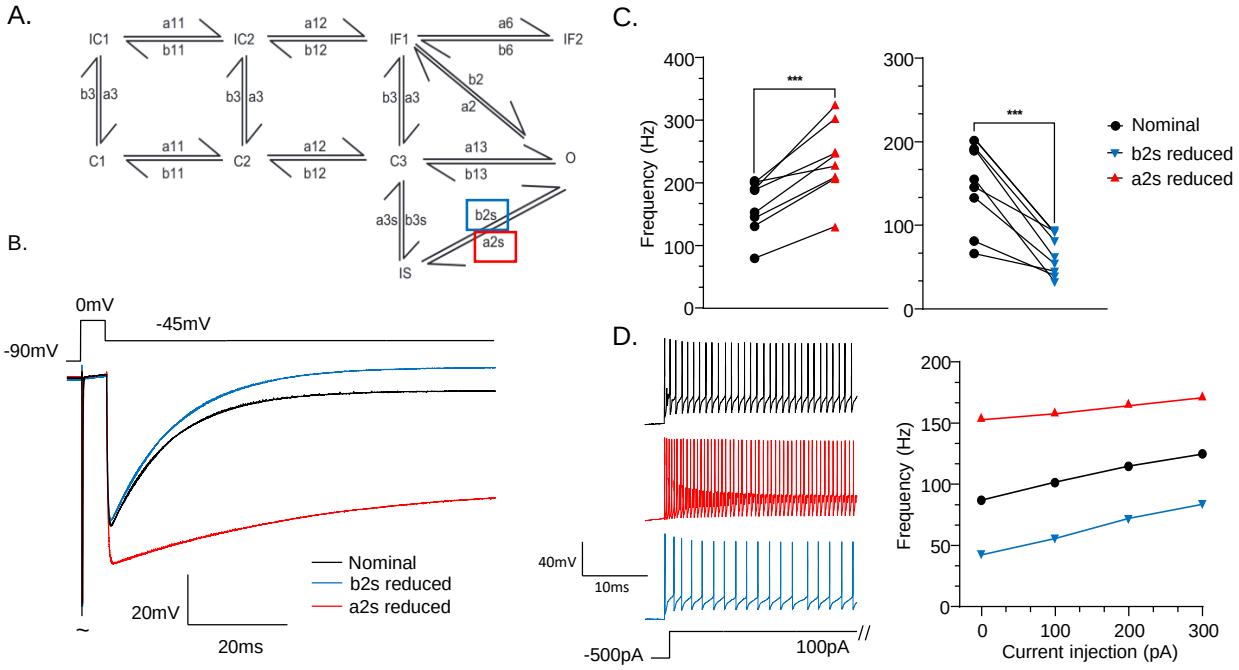

Table 1. Brown et al.

Variable	Nominal	τdecay Reduced	τdecay Increased	I_{NaR} Reduced	I_{NaP} Reduced
a11 var1	0.023989	0.02288	0.0234922	0.024273	0.017821
a11 var2	961.08	962.9323	955.288069	961.1444	955.74551
a12	856.13	861.1349	855.83844	855.6402	943.691619
a13	72.682	70.27949	75.02708	72.05751	45.1006
b11 var1	0.17233	0.13391	0.1957689	0.145184	0.162969
b11 var2	19.691	18.23159	18.08988	20.02451	17.5219955
b12	88.549	87.66816	90.404	88.7198	77.35325
b13	148.41	162.7141	230.9623	174.5183	160.84845
a3 var1	0.36734	0.514279	0.391971	0.308533	1.006506
a3 var2	980.34	964.714	979.85264	980.6689	985.713
b3 var1	53.241	53.5899	53.2644	53.28371	74.161099
b3 var2	14.204	13.08476	13.65378	14.39238	14.43037
a2 var1	87.852	84.88214	99.3117	87.57206	83.96448
a2 var2	999.72	998.5897	998.65724	999.7462	999.9939
a6 var1	609.21	589.9252	621.0904	610.1094	619.312417
a6 var2	86.49	84.00415	88.18935	101.533	96.412457
b6 var1	156.45	224.2441	150.19414	156.3997	147.127477
b6 var2	30.317	28.8311	39.98108	58.02996	56.26988
a2s var 1	15.817	37.25738	12.52364	15.71892	22.593552
a2s var 2	999.82	999.9025	999.95304	999.7914	987.9528
b2s var1	0.001001	0.001207	0.001026	0.001003	0.001002
b2s va2	11.963	10.81732	13.212289	11.96024	15.16399
a3s var1	0.00447733	0.001042	0.003335	0.005083	0.00100109
a3s var2	999.93	999.2872	999.97387	999.9429	999.97908

Where the transition rates are of the form: a11 = Tfactor*1/(Input(1)*exp(-V/Input(2))); a12 = Input(3)*a11; a13= Input(4)*a11; b11 = Tfactor*1/(Input(5)*exp(V/Input(6))); b12 = Input(7)*b11; b13= Input(8)*b11; a3 = Tfactor*Input(9)*exp(-V/Input(10)); b3 = Tfactor*Input(11)*exp((V)/Input(12)); a2 = Tfactor*(Input(13)*exp(V/Input(14)); b2 = ((a13*a2*a3)/(b13*b3)); a6 = Tfactor*(Input(15)*exp(V/Input(16))); b6 = Tfactor*Input(17)*exp(-V/Input(18)); a2s = Tfactor*(Input(19)*exp(V/Input(20)); b2s = Tfactor*(Input(21)*exp(-V/Input(22))); a3s = Tfactor*Input(23)*exp(-V/Input(24)); b3s = (a2s*a3s*a13)/(b2s*b13);
Q10 = 3; T = 295;
Tfactor = 1.0/(Q10^((37.0-(T-273))/10.0))

Table 2. Brown et al.

Model	Mean AP duration (100%) (μs)	Mean AHP (mV)	Mean AP Peak (mV)	Mean AP Threshold (mV)	Mean AP Amplitude (mV)	Max dV/dt (V/μs)
No model (n = 29)	411.8 ± 11.95	-73.10 ± 0.561	1.024 ± 1.089	-59.11 ± 0.546	60.14 ± 1.242	587.7 ± 20.35
Nominal (n = 29)	475.3 ± 13.20 (p < 0.0001)	-72.70 ± 0.615 (p = 0.4499)	5.662 ± 1.044 (p < 0.0001)	-56.86 ± 0.578 (p = 0.0026)	62.52 ± 1.329 (p = 0.0011)	582.2 ± 25.62 (p = 0.7291)
I_{NaP} Reduced (n = 37)	488.6 ± 11.82 (p = 0.0015)	-73.41 ± 0.588 (p = 0.9242)	5.544 ± 1.342 (p < 0.0001)	-57.08 ± 0.628 (p < 0.0001)	62.62 ± 1.720 (p < 0.0001)	573.7 ± 26.18 (p = 0.0001)
I_{NaR} Reduced (n = 35)	523.9 ± 33.22 (p = 0.0153)	-72.93 ± 0.755 (p = 0.6177)	5.769 ± 1.213 (p = 0.8196)	-56.60 ± 0.807 (p = 0.0022)	62.37 ± 1.513 (p = 0.6351)	555.3 ± 24.62 (p = 0.0282)
τ_{decay} Reduced (n = 34)	513.4 ± 17.43 (p = 0.0009)	-74.34 ± 0.501 (p < 0.0001)	10.93 ± 1.245 (p < 0.0001)	-58.84 ± 0.463 (p = 0.1665)	69.78 ± 1.410 (p = 0.0003)	670.6 ± 24.89 (p < 0.0001)
τ_{decay} Increased (n = 36)	497.9 ± 13.32 (p < 0.0001)	-73.48 ± 0.700 (p = 0.0601)	7.036 ± 1.320 (p < 0.0001)	-56.98 ± 0.717 (p = 0.0318)	64.02 ± 1.484 (p < 0.0001)	589.5 ± 24.63 (p < 0.0001)
HT I_{NaR} Reduced (n = 17)	488.3 ± 28.81 (p = 0.0183)	-72.50 ± 1.321 (p = 0.6783)	1.364 ± 1.046 (p = 0.9883)	-56.29 ± 1.812 (p = 0.2675)	57.65 ± 2.402 (p = 0.5275)	502.7 ± 33.32 (p = 0.0968)
HT I_{NaR} Increased (n = 15)	508.9 ± 50.16 (p = 0.2171)	-72.14 ± 1.498 (p = 0.3844)	3.745 ± 1.112 (p = 0.0281)	-52.79 ± 1.872 (p = 0.0088)	56.53 ± 1.817 (p = 0.2323)	478.4 ± 20.75 (p = 0.0005)

Supplemental Figure 1. Brown et al.

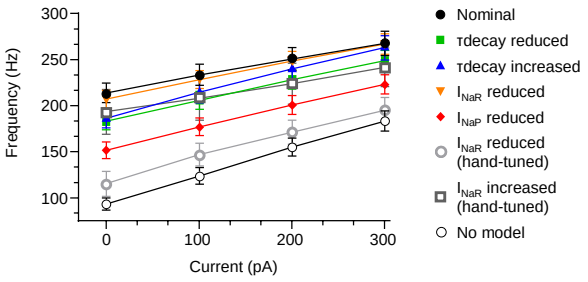

Supplemental Figure 2. Brown et al.

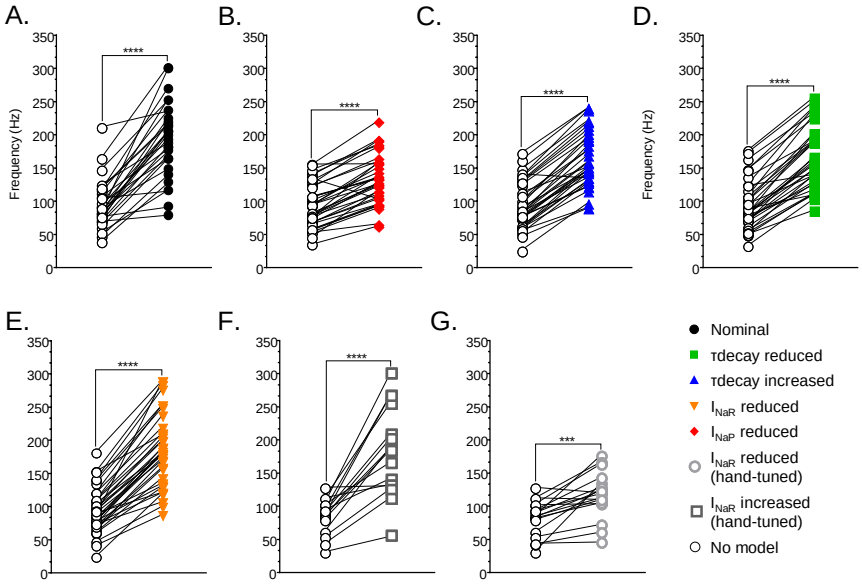
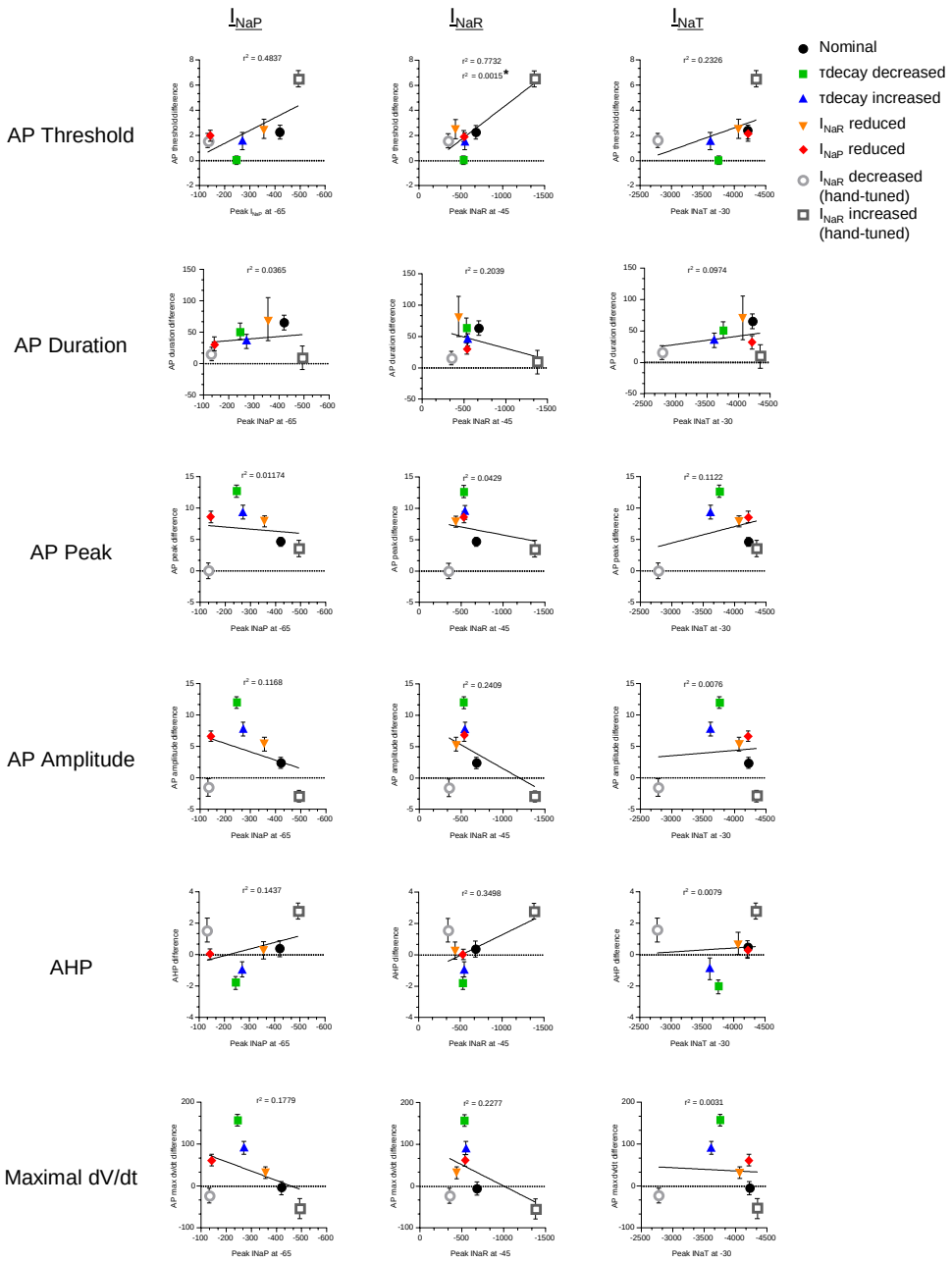
Supplemental Figure 3. Brown et al.